UNIVERSIDADE DA BEIRA INTERIOR
Engenharia

Low Reynolds Number Propeller Performance Measurement in Wind Tunnel Test Rig

Pedro Jorge Ferreira Alves

Dissertação para obtenção do Grau de Mestre em
Engenharia Aeronáutica
(Ciclo de Estudos Integrado)

Orientador: Prof. Doutor Miguel Silvestre

Covilhã, Outubro de 2014

“Don’t believe what your eyes are telling you. All they show is limitation. Look with your understanding, find out what you already know, and you’ll see the way to fly.”
Richard Bach, Jonathan Livingston Seagull

Acknowledgments

The present work was supported by European Union through the 7th Framework Programme applied to the Project MAAT (Ref. No. 285602). Part of the work was also supported by C-MAST - Center for Mechanical and Aerospace Sciences and Technologies, Portuguese Foundation for Science and Technology Research Unit No. 151.

Resumo

O objetivo do trabalho levado a cabo nesta tese foi dotar o túnel de vento da Universidade da Beira Interior de um equipamento de medição de desempenho de hélices de baixo número de Reynolds. Esta condição verifica-se em casos da aplicação em pequenos Veículos Aéreos Não Tripulados (VANTs) ou aeronaves que operem a grande altitude, como é o caso dos dirigíveis no projeto MAAT-Multybody Advanced Airship for Transport. O sistema de medição foi desenvolvido para recolher dados de desempenho de hélices com um diâmetro compreendido entre 6 e 14 polegadas (aprox. 0,15 a 0,40 m), operando num número de Reynolds compreendido entre 30.000 a 300.000 (baseado na corda a $3/4$ do raio da pá). O conceito escolhido para a estrutura da balança desenvolvida para a medição da tração, consiste num pêndulo em forma de *T* que se assemelha ao originalmente construído na Universidade de Illinois em Urbana-Champaign (UIUC). Devido ao posicionamento ajustável de célula de carga, esta configuração permite a utilização de toda a escala da célula de carga para a maioria das condições de funcionamento das hélices propostas. A conceção, construção e validação de todo o mecanismo e procedimentos de medição são apresentados detalhadamente. Além disso, foi medido o desempenho de duas hélices da gama *CAM Carbon* do fabricante *Aeronaut*, a de duas pás 13x8" e a de três pás 12x8". Foi demonstrado que, o aumento do número de Reynolds associado ao aumento das *RPM*, tem uma influência considerável no desempenho das hélices, aumentando a sua eficiência e coeficiente de tração. A instalação experimental desenvolvida pode ser utilizada para diversos fins, nomeadamente: o projeto de hélices no seio do Departamento de Ciências Aeroespaciais da UBI; para os trabalhos de desenvolvimento de VANTs, bem como para a validação e aperfeiçoamento de ferramentas numéricas como é o JBLADE.

Palavras-chave

Hélice de Baixo número de Reynolds, Teste de Hélices em Túnel de Vento, Balança de Tração e Torque.

Abstract

The objective of the work in this thesis was to to equip the University's of Beira Interior wind tunnel with a Low Reynolds Number (LRN) Propeller Performance Test Rig. This LRN condition is verified in small Unmanned Aerial Vehicles (UAVs) applications or in the high-altitude airships covered by the project MAAT-Multybody Advanced Airship for Transport. The design, construction and validation of an accurate measuring mechanism was conducted. The test rig was developed to collect performance data of propellers with diameter between 6 to 14 inches (approx. 0.15 to 0.40m), operating at Reynolds number between 30,000 to 300,000 (based on chord at $3/4$ of the blade radius). The design chosen for the thrust balance closely resembles the T-shaped pendulum structure originally built in the University of Illinois at Urbana-Champaign (UIUC). Due to the adjustable load cell positioning, this setting allows the use of the full range of the load cell for most thrust levels in the propeller size, relative wind speed and rotation speed ranges.
The test rig was completely validated and the experimental procedure was shown herein as well. Furthermore, thrust and torque characteristics of two Aeronaut Carbon Electric were measured. It was shown that as the Reynolds number increases with the increase of propeller *RPM*, it affects the propellers performance increasing their thrust coefficient and their efficiency. The developed test rig can be used for several purposes, namely: the design of propellers in the UBI's Department of Aerospace Sciences; the development UAVs, as well as the validation and improvement of numerical tools such as JBLADE.

Keywords

Low Reynolds Propeller Performance, Wind Tunnel Test Rig, Thrust and Torque Balance.

Contents

List of Figures

List of Tables

List of Acronyms

UBI	University of Beira Interior
BEM	Blade Element Momentum
CAD	Computer-Aided Design
EP	Electric Propulsion
FS	Full Scale
LRN	Low Reynolds Number
LVDT	Linear Variable Differential Transformer
PID	Proportional-Integral-Derivative
RPM	Revolutions per Minute
UAV	Unmanned Aerial Vehicles
UBI	University of Beira Interior
UIUC	University of Illinois at Urbana-Champaign
WWII	World War II

Nomenclature

A	propeller disk area, m^2
A_1	wind tunnel settling chamber cross-sectional aera, m^2
A_2	wind tunnel test chamber cross-sectional aera, m^2
C	jet cross-sectional area, m^2
C_D	drag coefficient
C_P	power coefficient
C_T	thrust coefficient
D	propeller diameter, m
d	maximum bending deflection, mm
$D_{fixture}$	motor fixture drag, N
E	Young's modulus, MPa
η	efficiency, %
I	moment of inertia, mm^4
J	propeller advance ratio
L	profile's length, mm
n	rotation speed, rev/s
N	number of acquired samples
P	power, W
P_{atm}	atmospheric pressure, Pa
p_1	static pressure at wind tunnel settling chamber, Pa
p_2	static pressure at wind tunnel test chamber entrance, Pa
Q	torque, $N.m$
R	ideal gas constant, $J/mol.K$
ρ	air density, kg/m^3
S	frontal area, m^2
σ	standard deviation
T	thrust, N
T_{atm}	atmospheric temperature, K
U	corrected freestream velocity, m/s
V	raw freestream velocity, m/s

Chapter 1

Introduction

1.1 Importance of Propeller Performance Data

Any new aircraft design have to meet specific performance requirements. To achieve this objective, it is necessary that each part of the aircraft be as efficient and serviceable as possible while taking into consideration such factors as weight and volume. Propeller selection is a key factor to achieve a good propulsion system, which makes the availability of the propeller performance data a critical issue to reach a successful design. Experimental work on propeller performance was abundant before WWII [1, 2] and a database of propeller performance characteristics got established. That was the golden age of propeller driven aircraft. After WWII, the widespread of jet propulsion limited the use of propellers to light aircraft. However, in recent times, the small Unmanned Aerial Vehicles (UAV) advent has triggered the interest in the Low Reynolds Number (LRN) wing and propeller aerodynamics. LRN effects can decrease the performance of propellers and the ability of the available numerical methods to predict that performance. To deal with this, JBLADE [3] software is being developed, as an open-source propeller design code, using a modified [4] Blade Element Momentum (BEM) theory which accounts for three dimensional flow equilibrium. The software is coupled with XFOIL [5] for its suitability in predicting LRN airfoil performance [6]. JBLADE will be used to design different propellers as well as to estimate their off-design performance. To improve the prediction capability of JBLADE, accurate LRN propeller performance data is needed.

1.2 State of the Art

1.2.1 Thrust Measuring Mechanisms

Electric propulsion (EP) systems provide high specific impulse, but low thrust, relative to chemical systems [7]. While the high thrust propulsion systems are accurately tested with simple load cells implementations, the low thrust EP devices require a more sensitive measuring mechanisms, typically called thrust balances or thrust stands. Many different design approaches exist for this thrust balances, however most of them can be generally classified into two main categories: the pendulum style and the torsional style [7]. The pendulum style type thrust stands are being considered both hanging and inverted. In the hanging pendulum configuration, the thruster sits on a platform that hangs from an arm attached to a base by a pivot point of known stiffness. This design is inherently stable because any oscillations that it experiences are damped out by gravity [8]. The inverted pendulum thrust stands are less stable, and hence more sensitive than the hanging pendulum [7] since on this configuration the gravity works against the torque from the pivot rather than with it. Contrary to what happen with both pendulum configurations, the restoring force in the torsional configuration (which rotates about an axis that is parallel to the gravity vector) can be made independent of the thruster mass [7].

1.2.2 Examples of Reference Applications

In 1990, Asson [9] provided a mechanical assembly capable of simultaneously measure the thrust and torque for several propellers. His main objective was the study of propellers, whereby the motor was kept the same in all the tests. The thrust measurement was performed by an Linear Variable Differential Transformer (LVDT).

The test rig purposed by Merchant [10] in 2004 consists on a FUTEK two-component load cell mounted on and supported by a C-structure and a solid steel adapter, that give to the entire fixture a firm foundation. This apparatus has a multi-motor adapter designed to accommodate a large range of motors that increase the range of propeller diameters which can be tested.

According to the measuring model proposed by Rozehnal [11] in 2007, the experimental equipment is located in the circulation wind tunnel with the open testing area (see Figure 1.1). The measuring system is fully automated in order to measure both static and dynamic propeller aerodynamic characteristics.

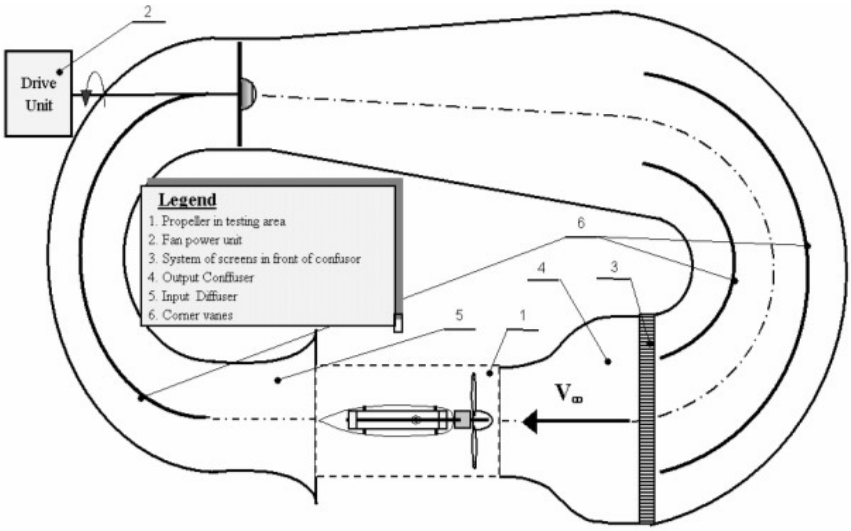

Figure 1.1: Scheme of the wind tunnel with the propeller test rig in open testing area proposed by Rozehnal [11].

In 2008, Uhlig [12] used an experimental setup originally developed by Brandt and Tehrani [13] that consists on a pendulum supporting the torque cell and the motor-propeller assembly in the centre of the wind tunnel. This arm is extended outwards of the wind tunnel, allowing the transfer of the force to a load cell through a second arm. The arm located inside the wind tunnel is protected with a symmetrical profile fairing to reduce the rig drag and therefore the amount of interferences in the thrust measurement. This balance was designed in order to allow 10 different locations for the load cell. The position of the load cell is properly changed according to the expected thrust that the propeller will produce during the tests. This procedure allow the use of the full scale of the load cell, which in turn, allow more accurate measurements. This test rig has also being used by Deters and Selig [14] during their experimental work [15].

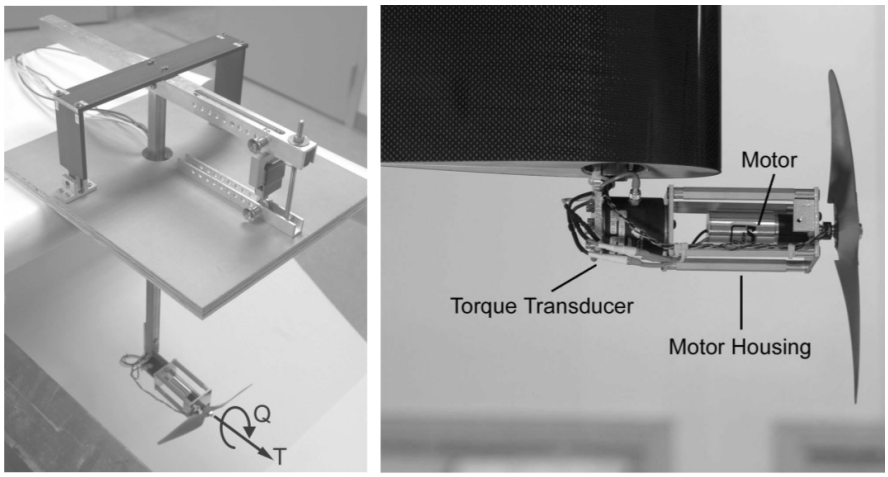

Figure 1.2: Experimental setup used by Uhlig [12]. (a) Without faring. (b) In-detail motor fixture assembly.

In Kotwani's [16] setup, thrust is measured by a load cell subjected to a bending moment. The motor is fixed in the horizontal position in one of the ends of the test rig, whereas the other end is fixed to a rigid support structure as described in Figure 1.3.

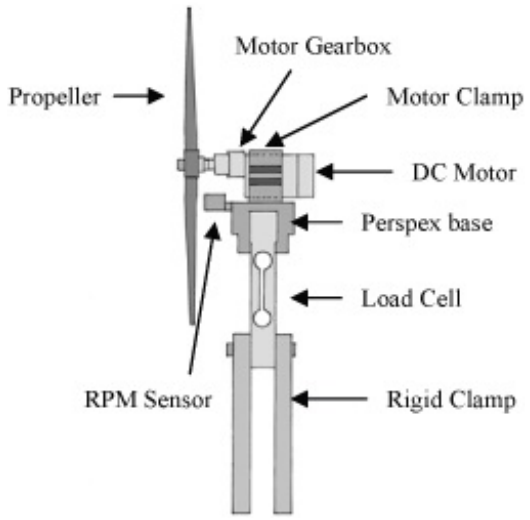

Figure 1.3: Thrust measuring mechanism purposed by Kotwani [16].

1.3 Motivation for the Thrust Balance Redesign

The laboratory already had a working thrust measuring mechanism developed in 2011 by UBI graduate student Ricardo Salas [17]. This system was based on the use of a hybrid cell combining thrust and torque measurements. The experimental apparatus was able to collect propellers performance data but had an implementation flaw which is the uncertainty of the measurements, since the magnitude of the highest measured forces and moments was much less than the Full Scale (FS) of the used cell (approx. 3% of the thrust FS and 30% of the torque FS). One

of the desired improvements was the independence between thrust and torque cell's FS allowing us to chose the right (thrust and torque) measuring setup simultaneously. Furthermore, the apparatus implemented by Salas [17] had a large frontal area, disturbing the flow and affecting the validity of measured quantities. In addition, the design proved to be inaccurate for this lower magnitudes of thrust and torque outputs.

1.4 Goals

The main goal of the work carried out during this thesis was to equip the University's of Beira Interior wind tunnel with a Propeller Performance Test Rig. The design, construction and validation of an accurate measuring mechanism was conducted. The new test rig must be sufficiently sensitive and capable of collecting performance data of propellers with diameter between 6 to 14 inches (approx. 0.15 to 0.40m), operating at Reynolds number between 30,000 to 300,000 (based on chord at $3/4$ radius and sea level conditions). This document describes the concepts used in the developed system, its features, the design itself, the validation and the obtained results.

Chapter 2

Methodology

2.1 Design of the Thrust and Torque Balance

In this section the design method for the thrust and torque balance is described. Firstly, the project requirements are presented and discussed. Subsequently, the sizing and construction steps, including the selection of components such as flexural pivots, load and torque cells are presented. The *CAD* models, the control mechanism, used hardware and software are presented thereafter. Finally, the designed calibration mechanisms are shown.

2.1.1 Design Requirements

The design requirements of the balance are based on the following objectives:

1. The balance must be designed such that can be used in the wind tunnel, located in the laboratory of Aerospace Sciences at the University of Beira Interior replacing an older measuring device. This means that it needs to be sized to ensure it's dimensional compatibility with the facilities;
2. The system must be movable in order to use the wind tunnel for other purposes than propeller performance data acquisition;
3. The propeller's position should be as close to the centre of the test volume as possible;
4. The system must be able to accurately measure a propeller's thrust and torque;
5. A 0.15m to 0.36m (6 to 14 inch) propeller can be tested;
6. The system has to have a high measurement sensitivity. Through experimental results available [15], for the established range of propeller diameters (6" to 14"), thrust values up to 15N are expected. The hybrid cell used in the old measuring system has a Full Scale of 0-500N with an uncertainty of +/- 1N (at least 7 % of this thrust magnitudes). With this new measurement system is desirable to ensure a maximum uncertainty of +/- 0.1N;
7. The experimental apparatus must be free of any sources of friction in order to have the minimum interference with the measured quantities;
8. The data acquisition system should be as autonomous as possible.

2.1.2 Design Concept

The design chosen for the thrust balance closely resembles the T-shaped pendulum structure originally built in University of Illinois at Urbana-Champaign (UIUC) [18], but modified to meet the design requirements presented in Section 2.1.1. An initial sketch of the concept is shown in Figure 2.1. Due to the adjustable load cell positioning, this setting allows the use of the full range of the load cell for most thrust levels in the propeller size, relative wind speed and

rotation speed ranges. In addition, an effort was made to reduce the complexity of the assembly inside the wind tunnel, in order to ensure minimal flow and measuring disturbances. The T-shaped pendulum is pivoted about two flexural pivots (see Figure 2.1) while being constrained by a load cell outside of the tunnel in an area above the test volume where plenty of room is available. The flexural pivots are frictionless bearings, designed for applications with limited angular travel. This devices are stiction-free bearings with negligible hysteresis. The pivots are made with flat, crossed springs, that visually appear like a cross-hair, supporting rotating sleeves. These flexural pivots were chosen over the standard bearings since they greatly reduce the adverse tendencies that bearings are prone to, when used in static applications, namely stiction and hysteresis.

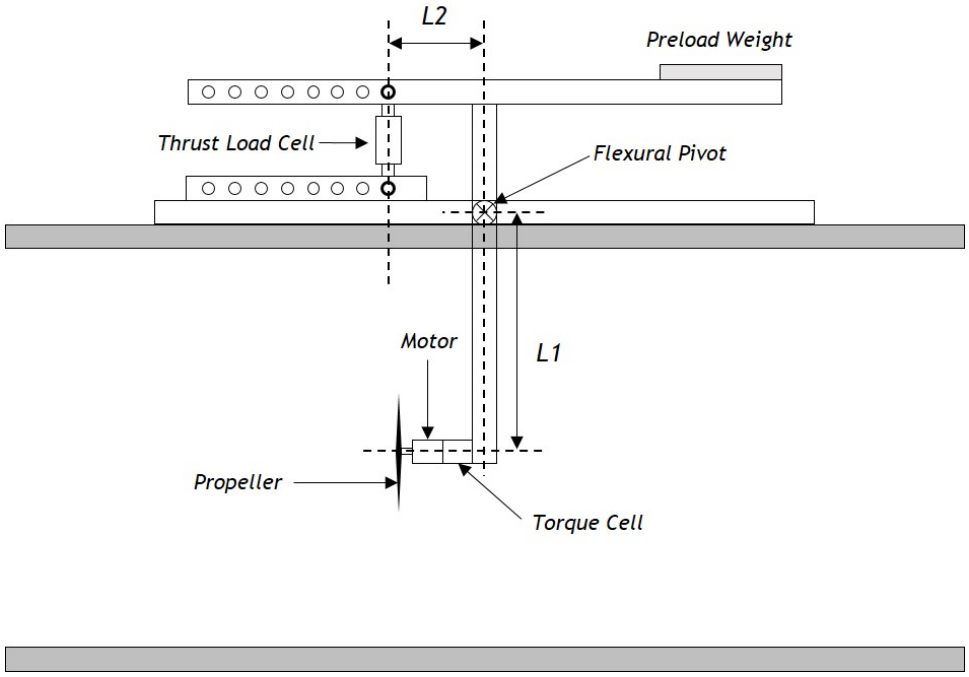

Figure 2.1: Initial sketch of the thrust and torque balance design concept.

2.1.3 Pre-existing Infrastructure

In order to proceed with the structure sizing, a realistic 3D *CAD* model of the test volume and pre-existing infrastructure was made in CATIA V5. The tunnel has support bars over the outer section of the test volume as can be seen in Figure 2.2. These bars were used as support for the torque and thrust balance.

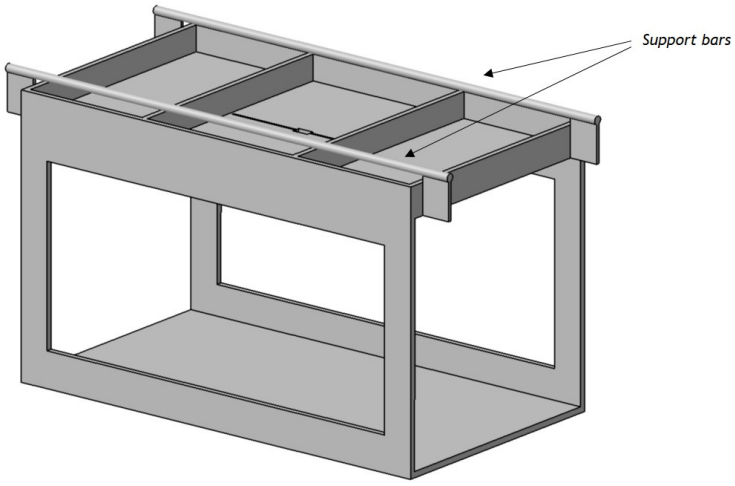

Figure 2.2: 3D *CAD* model of the tests volume structure of UBI's wind tunnel.

2.1.4 Balance Chassis

After some iterative design the structure illustrated in Figure 2.3 was obtained. This modular assembly concept allows almost integral changes, if required in the future, being ready to receive new features.

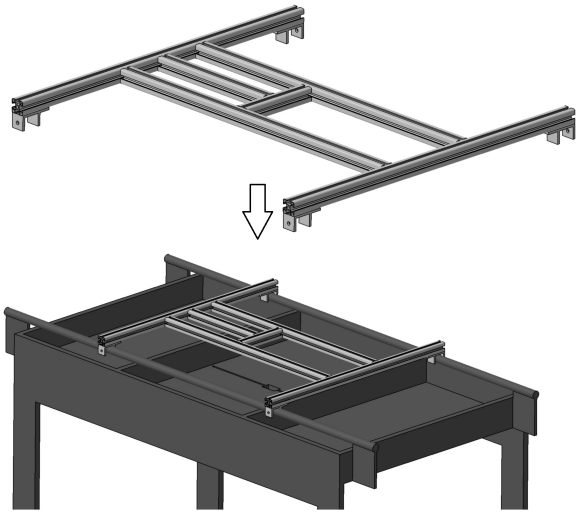

Figure 2.3: Balance Support Structure.

Due to its versatility, the aluminium *MINITEC* profiles were chosen to the chassis. This type of profile is quite popular in the industry because it allows modular assemblies. The profile chosen was the *MINITEC 30x30* whose the characteristics are shown in Figure 2.4.

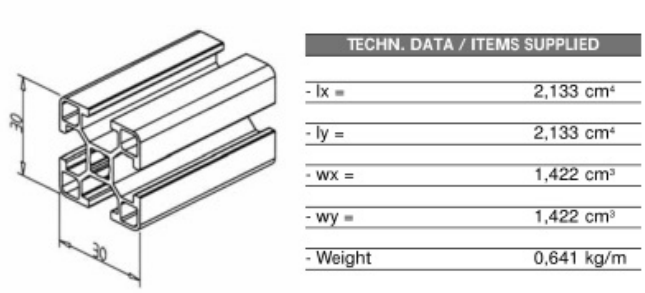

Figure 2.4: *MINITEC 30x30* aluminium profile specifications.

2.1.5 Balance Pendulum Structure

The pendulum was designed in order to have the thrust vector located at the centre of test section. Another design concern was to ensure that there will be enough space for assembling the load cell and its accessories above the wind tunnel upper wall. In Figure 2.5 the pendulum main dimensions are illustrated. The next step was to select the aluminium profile for the structure. Since the pendulum's vertical arm will be loaded with the thrust force (as shown in Figure 2.1), it will be subjected to bending moments. Thus, we had to carefully check the suitability of the profile for this structure. Regarding the structure, three different profiles were chosen: *MINITEC 30x30*, *MINITEC 19x45* and *MINITEC 19x32* (see Figure 2.6) for further analysis of the loading caused by the propellers thrust. The first step was to analyse what would be the maximum expected thrust for the propellers that may be tested. Due to the 0.8mx0.8m dimensions of the test section, it was decided to limit the maximum diameter of the propellers to be tested at 14". Using the data found at the propeller performance database provided by UIUC [15], we concluded that for 14" propellers, in static conditions (worst case scenario), the maximum measured thrust is close to 15N.

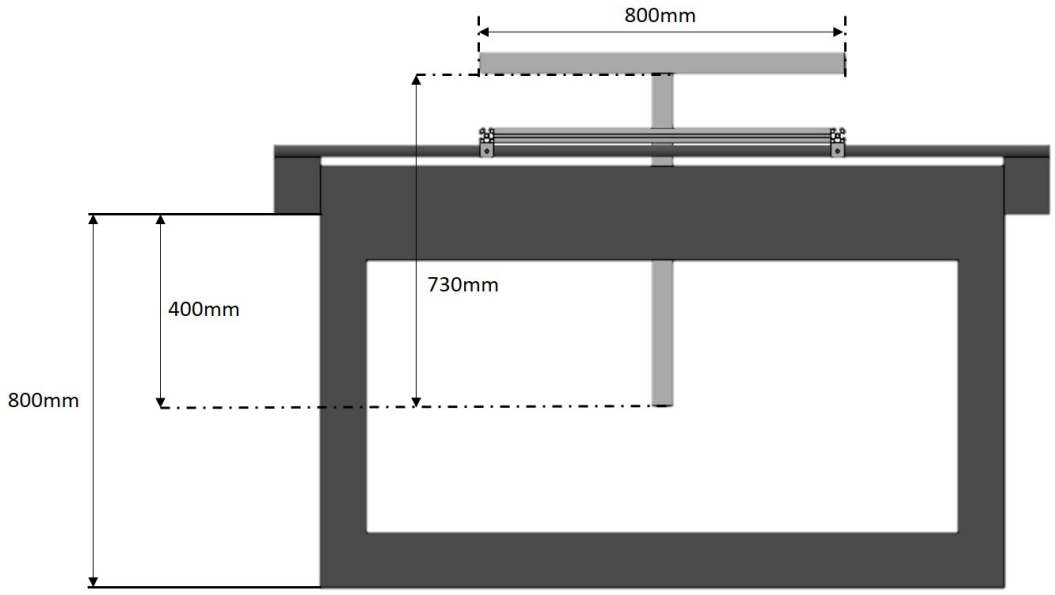

Figure 2.5: Balance Pendulum Main Dimension.

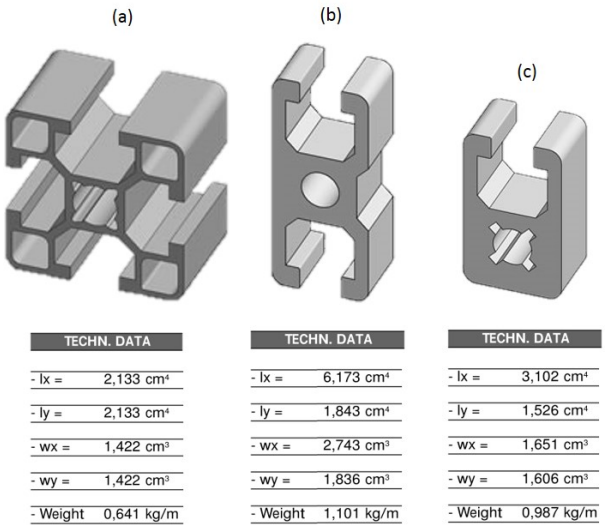

Figure 2.6: Chosen aluminum profiles for analysis.
MINITEC 30x30(a); *19x45*(b); *19x32*(c).

The maximum bending deflection of each profile can be calculated with the information provided in the *MINITEC Catalogue* [19] according the Eq. 2.1.

$$d = \frac{T \times L^3}{3 \times E \times I \times 10^4} \quad (2.1)$$

where T is the thrust force, L the length of the profile, E the material's Young's modulus and I the profile moment of inertia.

From Figure 2.5 $L = 730mm$, knowing that $I_{30\times30} = 21330mm^4$, $I_{19\times45} = 61730mm^4$ and $I_{19\times32} = 31050mm^4$ and varying the thrust force from 0 to 15N, the deflection for each profile was calculated. The results are shown in Figure 2.7 and, as expected, the profile with the highest moment of inertia (*MINITEC 19x45*) experiences the lowest deflection at its end (all the presented dimensions are in mm).

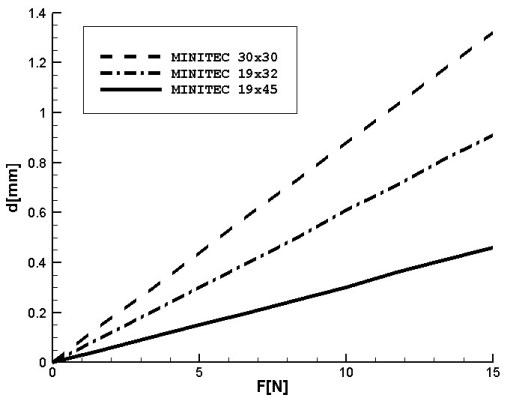

Figure 2.7: Deflection of the possible profiles under the maximum load thrust.

2.1.6 C-structure Interface

In order to join the pendulum to the flexural pivots, it was also necessary to develop an interface between these components. In Figure 2.8, the structure for this task is presented. The interface has a “C-shape” and hosts the moving part of the flexural pivots.

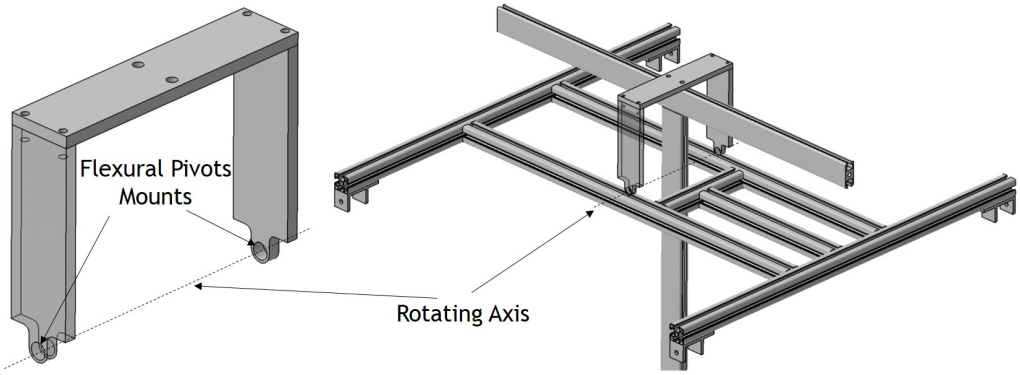

Figure 2.8: C-structure used to interface the pendulum to the chassis.

This structure was built using stainless steel and it is built with three 9mm thick plates bolted together. Figure 2.9 shows the interface between the C-structure and the chassis as well as the positioning of the flexural pivots. Due to the dimensional accuracy required and the type of material (stainless steel), these components were laser cut by a specialized company. The mechanism to hold the flexural pivots was designed according to the application recommendations published by the manufacturer [19]. To place the flexural pivots, the hole diameter should be between 0.0005 to 0.0015 inch (0.013 to 0.038mm) larger than the pivot diameter. In case that vibration is expected, as herein, standard-locking methods should be used on the implemented method (clamping screw as seen in Figure 2.9). According to this procedure, the rotation axis about which the pendulum experiences angular movement coincides with the centre axis of the flexural pivots.

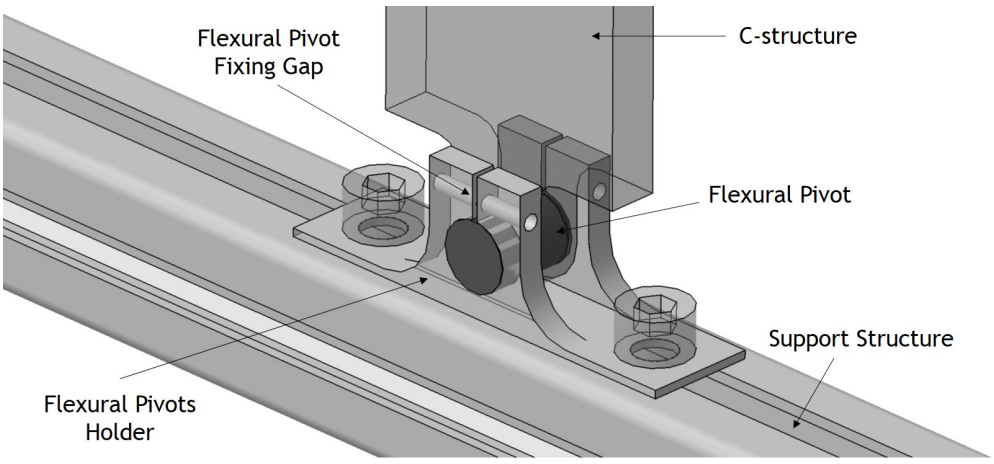

Figure 2.9: Flexural pivot holder and interface of the C-structure with the chassis.

2.1.7 Load Cell Variable Positioning

One of the key concepts for the assembly’s sensitivity is the possibility to adjust the position of the load cell along the upper arm of the pendulum. Thus, it becomes possible to use the

full range of the load cell for different intervals of propeller's produced thrust. The Figure 2.10 shows the system sketch, such that the distance $L2$ can be adjusted between 80 and 350mm in 10 increments of 30mm each.

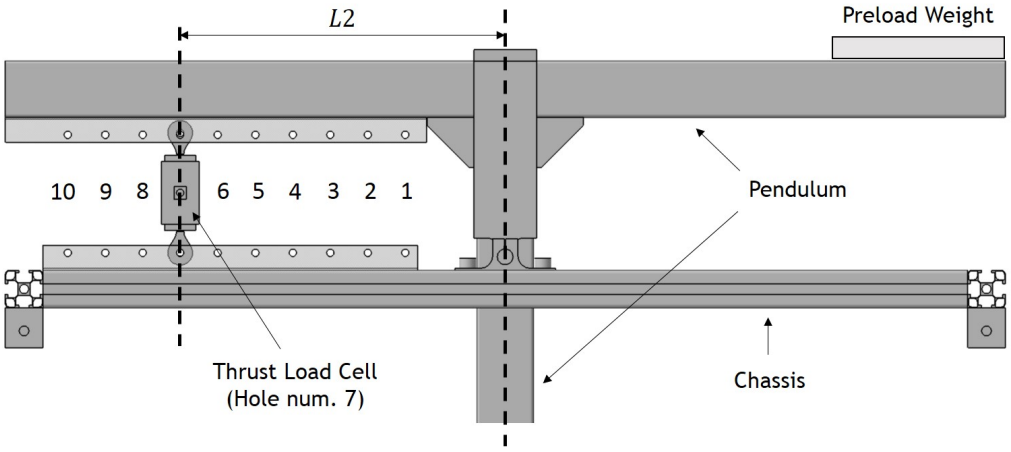

Figure 2.10: Scheme of the adjustable thrust load cell positioning.

The two quantities involved in the ratio between lower and upper arms for the different $L2$ distances is shown in Figure 2.1. This ratio, AR, is given by $L1/L2$. Considering the holes numbering as presented in Figure 2.10 and since the 10 different positions of the load cell are known, AR can be calculated as a function of $L1$ and the hole number, N_{hole}, as presented in Eq. 2.2.

$$AR = \frac{L1}{50 + (N_{hole} \times 30)} \quad (2.2)$$

The length of $L1 = 600mm$ was accurately defined in the 3D *CAD* model and implemented in the cut profiles. The table 2.1 summarizes the AR values given by Eq. 2.2 according to the position of the load cell. The load cell assembly is made through 2 compatible ball joints (model R3556.R006 from Automotion Component, UK). Initially, two M6 stainless steel rods and were used to secure the ball joints to the pendulum and chassis, but after running the first instrumented tests, these rods had to be replaced by nylon ones because they were originating interference with the load cell signal reading.

Table 2.1: $L1/L2$ arms ratio values as function of the load cell position hole number.

N_{hole}	$L1/L2$
1	7.50
2	5.45
3	4.29
4	3.53
5	3.00
6	2.61
7	2.31
8	2.07
9	1.88
10	1.71

2.1.8 Preload Weight

A preload weight was added to the balance on the opposite side to the load cell as shown in Figure 2.1. This preload weight kept the load cell in tension throughout propeller testing to make sure the load cell would not slip during negative thrust conditions.

2.1.9 Motor and Torque Transducer Attachment

In order to ensure proper assembly of the motor, the torque transducer and the pendulum, two adapter disks were developed (see Figure 2.11). One of these two adapters links the pendulum structure to the torque transducer whereas the other holds the motor to the torque transducer. These adapters have to withstand the torque and thrust loads that are produced by the propeller as well as the supported component's weights.

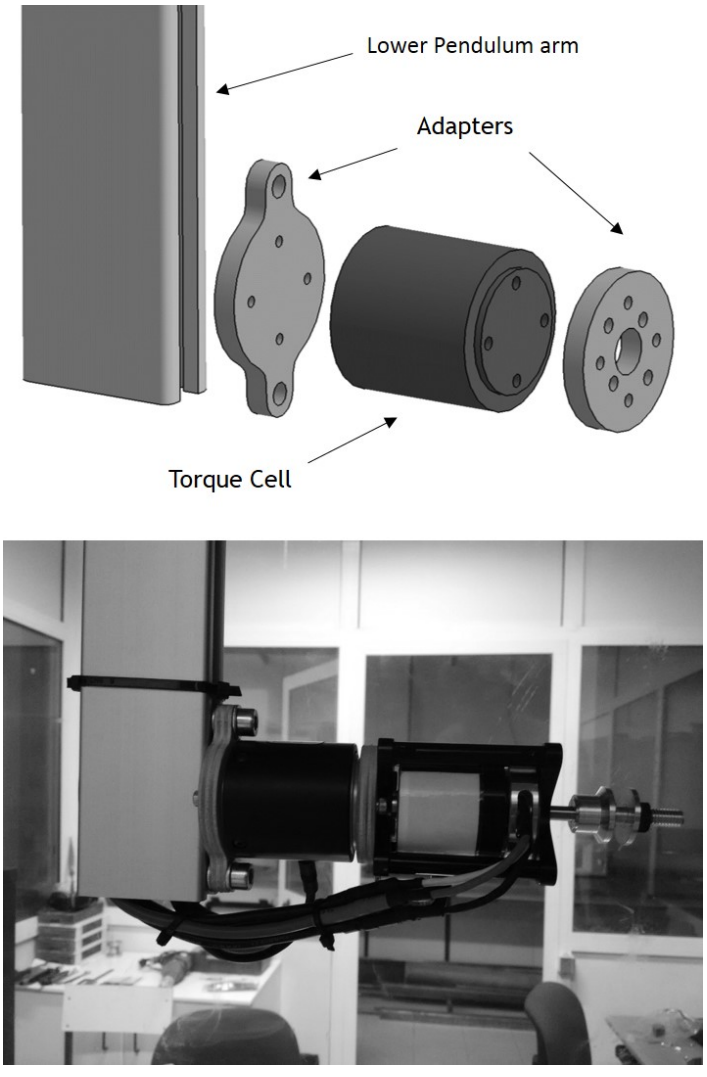

Figure 2.11: Scheme (top) and a photograph (bottom) of the assembly between the motor and torque transducer to the pendulum structure.

2.2 Experimental Setup

The experimental setup system can be divided into three subsystems, namely, the Propeller Balance, Signal Conditioners and the Data Acquisition System. Both, Signal Conditioners and Data Acquisition System, were originally designed by Pedro Santos [20]. However, in order to set up the new balance and new sensors, changes had to be made to the hardware and software previously existing.

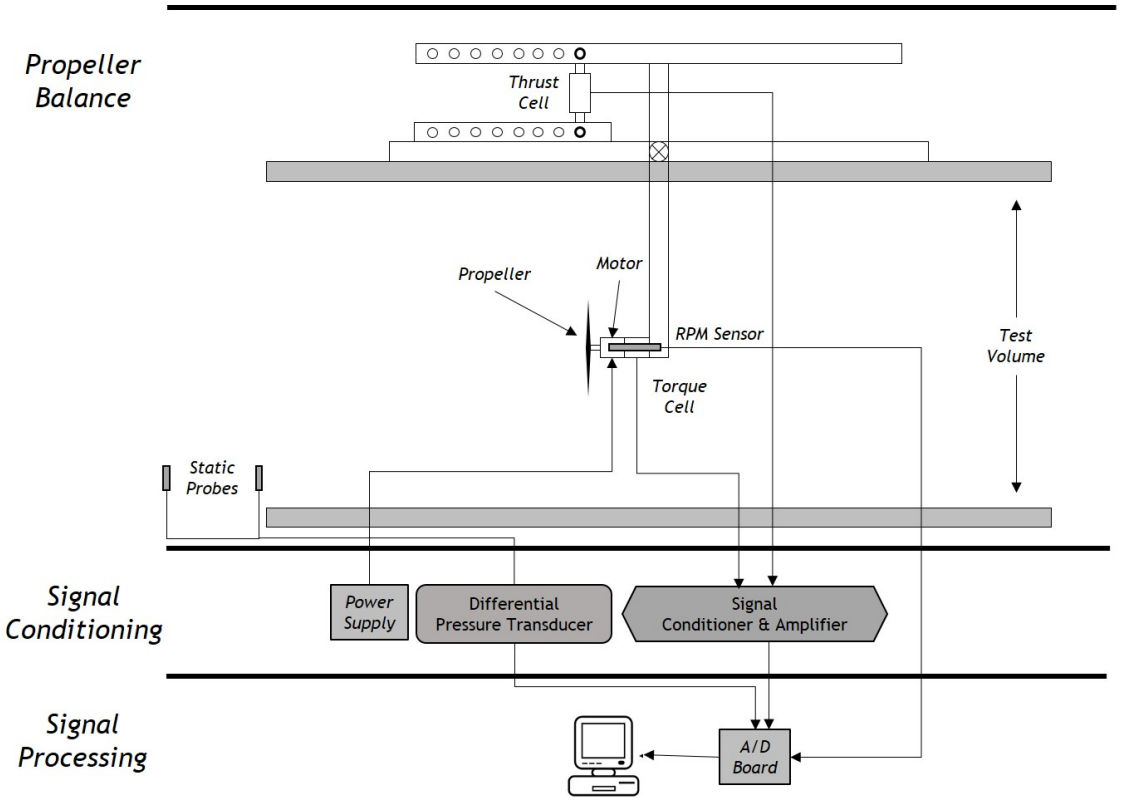

Figure 2.12: Measurement System Schematic Overview.

2.2.1 Thrust and Torque Measurement

The thrust load cell used is the FN3148 manufactured by *FGP Sensors & Instrumentation* having a maximum capacity of 100N. The torque produced by the propeller is measured using the RTS-100 and RTS-200 reaction torque transducers made by Transducer Techniques according to the torque level of the propeller being tested. Both thrust and torque load cells are connected to a high-precision strain gauge converter from *mantracourt*, model SCB-68, that converts a strain gauge sensor input to a digital serial output. In Figure 2.13 the specifications of thrust and torque cells are presented.

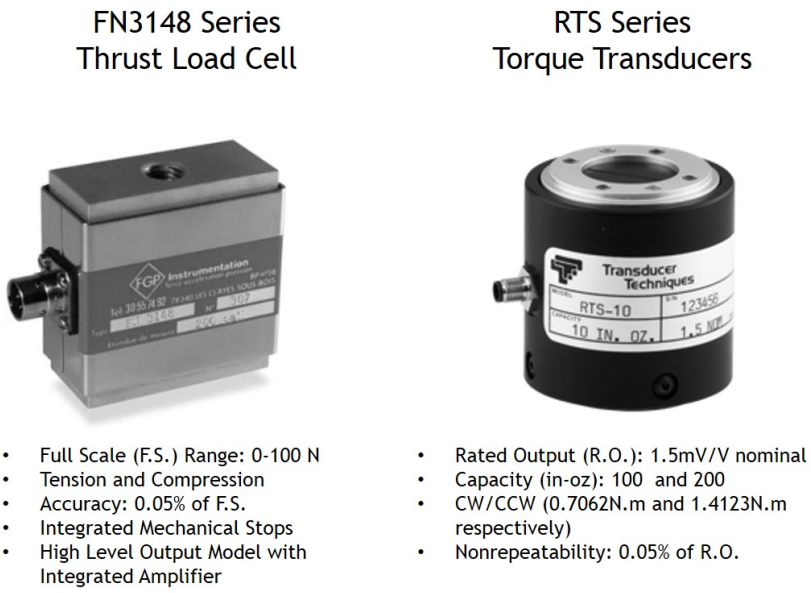

Figure 2.13: Balance Thrust and Torque sensors.

2.2.2 Propeller Speed Measurement

To measure the propeller rotation speed, a Fairchild Semiconductor QRD1114 photo-reflector was used to count the number of revolutions the output shaft makes in a fixed time interval (0.75s), resulting on an accuracy of $\pm 0.5 Rev/0.75 sec$. This sensor is constituted by two distinct parts: an infrared emitting diode and a phototransistor. A simple circuit composed by a limiting resistor (R1), a bias resistor (R2) and a Schmitt trigger is used. The former is used, as the name suggests, to limit the current to the infrared diode. The bias resistor is used to produce an output on the phototransistor side. The output of the phototransistor is further cleaned and digitized using a Schmitt trigger. The latter component is essential in order to make the output relatively independent of the distance from the reflecting surface.
Using this circuit, the sensor can be placed up to 2mm away from the reflective surface. The output voltage is near 0.27V when aimed at a white surface and about 4.61V when pointed at a black surface. The circuit has a response time of around $50 \mu sec$. The output voltages and response time of the circuit proved to be more than sufficient for measuring the rotational speed of the propellers, which never exceeded 7000 RPM in the validation tests presented in Chapter 3. This propeller speed measurement solution was also designed by Pedro Santos [20].

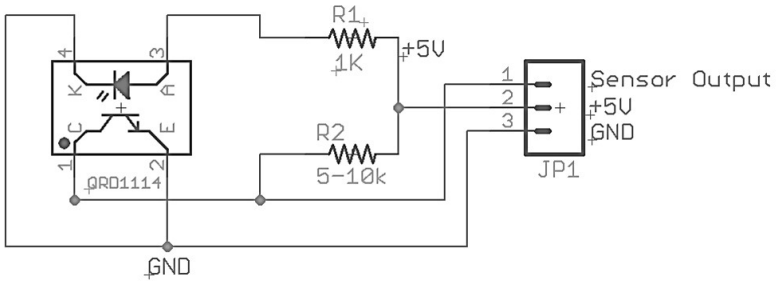

Figure 2.14: Photoreflector circuit schematic designed by Pedro Santos [20].

2.2.3 Freestream Velocity Measurement

The freestream velocity is measured with a differential pressure transducer, an absolute pressure transducer, and a thermocouple. In the previous installation [17], the dynamic pressure was measured with a pitot-static probe as shown in Figure 2.15. With this measuring method,

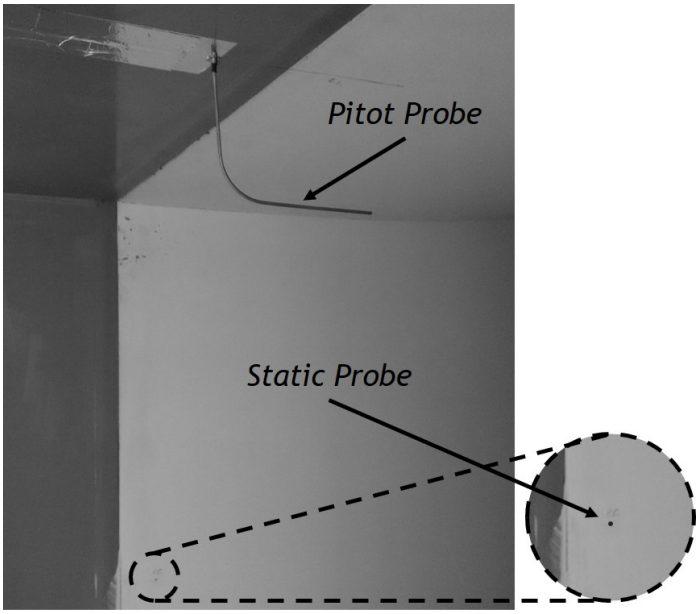

Figure 2.15: Previous pitot-static probe apparatus.

velocity corrections had to be applied to account for the changes in the freestream airspeed at the pitot tube section position created by the propeller. These corrections are complex and prone to wrong speed measurements [21]. The new measuring mechanism uses two static pressure ports, one at the tunnel settling chamber and another at the entrance of the test chamber as it is presented in Figure 2.16.

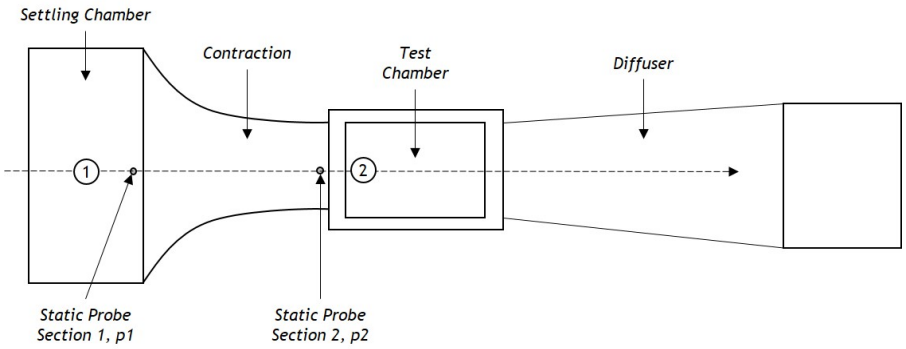

Figure 2.16: New freestream flow speed measuring mechanism.

The contraction section makes the velocity rise and the pressure fall at the test chamber (2). The pressure difference across is a measure of the flow rate through the tunnel.
The Bernoulli's equation gives:

$$\frac{p_1}{\rho} + \frac{1}{2}{V_1}^2 + gz_1 = \frac{p_2}{\rho} + \frac{1}{2}{V_2}^2 + gz_2 \quad (2.3)$$

Considering that the tunnel is horizontal, $z_1 = z_2$ 2.3 can be rewritten as:

$$V_2{}^2 - V_1{}^2 = \frac{2(p_1 - p_2)}{\rho} \quad (2.4)$$

and relate the velocities from the incompressible continuity relation:

$$A_1 V_1 = A_2 V_2 \quad (2.5)$$

or

$$V_1 = \frac{A_2}{A_1} V_2 \quad (2.6)$$

Combining 2.4 and 2.6, we obtain a formula for the velocity in the test section:

$$V_2 = \sqrt{\frac{2(p_1 - p_2)}{\rho\left[1 - \left(\frac{A_2}{A_1}\right)^2\right]}} \quad (2.7)$$

The atmospheric pressure outside of the tunnel is measured with an absolute pressure transducer made by Freescale Semiconductor model MPXA4115A. The temperature is measured with a National Instruments LM335 thermocouple located at the inlet of the wind tunnel as shown in Figure 2.17.

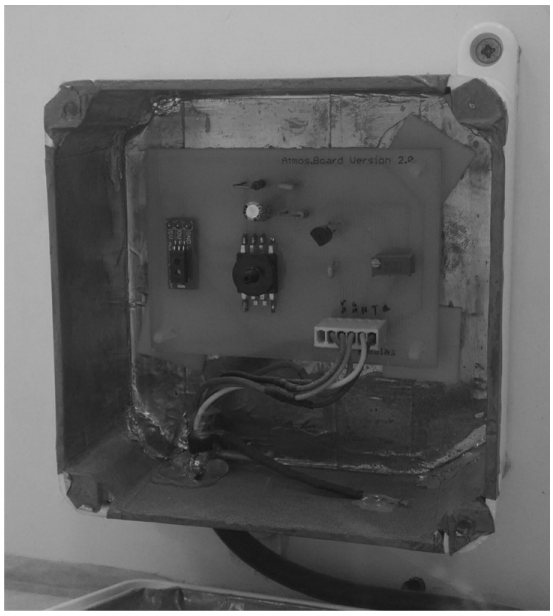

Figure 2.17: Absolute pressure, Humidity and Temperature sensors PCB's.

To validate this new freesteam velocity measurement method, two runs were performed with the test chamber empty, comparing the measurements with pitot-static probe to those with the two static probes as function of the wind tunnel *RPM* setting. Considering the obtained results, plotted in Figure 2.18, this new measuring method proved to be reliable, presenting less than 1% difference between the two measuring methods for all *RPM* settings that were analysed. This new method is also independent of possible inaccurate installations regarding the correct direction of the pitot probe as it uses the pre-installed wind tunnel static pressure ports.

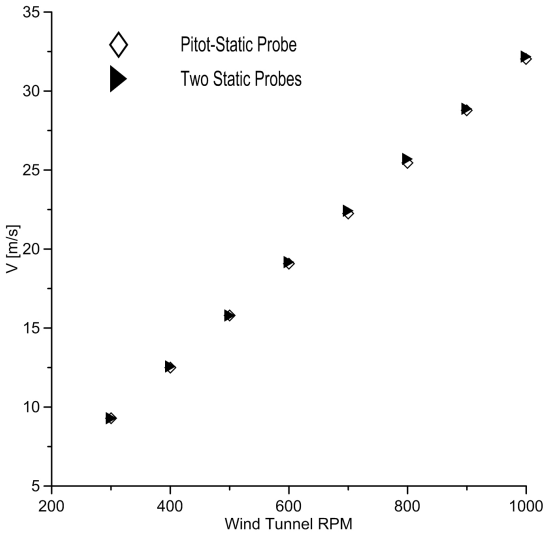

Figure 2.18: Measured freestream flow velocities as function of the wind tunnel *RPM*.

2.3 Variables and Propeller Performance Parameters

Variables can be divided into two categories, namely measured and calculated variables. The measured variables are directly obtained from the measurement instruments. Physical measurements of thrust, torque, rotational speed, static pressures, atmospheric pressure, and temperature are gathered. From these quantities, propeller power and the air density are calculated according to:

$$P = 2\pi n Q \quad (2.8)$$

$$\rho = \frac{P_{atm}}{R T_{atm}} \quad (2.9)$$

The wind tunnel freestream velocity was calculated according to the Eq. 2.6 as explained in section 2.2.3. Finally, the above measured and derived quantities are non-dimensionalized to obtain the propeller performance data. These quantities include the thrust coefficient (C_T given by Eq. 2.11), power coefficient (C_P given by Eq. 2.12), and efficiency (η given by Eq. 2.13). Static condition tests, where the advance ratio is zero ($J = 0$, see Eq. 2.10), were not presented in this thesis due to the fact that, to replicate the static condition, the wind tunnel test chamber's doors had to be opened, otherwise the propeller will be affected by the condition described in Subsection 2.4.1. Further testing under these conditions had to be performed in order to evaluate the reliability of the static tests inside the wind tunnel. For the non-static case ($J > 0$, see Eq. 2.10), the coefficients and the efficiency are plotted against the advance ratio. The definitions for the advance ratio, thrust and power coefficients, and propeller efficiency are given by

$$J = \frac{U}{nD} \quad (2.10)$$

$$C_T = \frac{T}{\rho n^2 D^4} \quad (2.11)$$

$$C_P = \frac{P}{\rho n^3 D^5} \quad (2.12)$$

$$\eta = J\frac{C_T}{C_P} \quad (2.13)$$

Where, U is the freestream velocity; D is the propeller diameter; T is the propeller thrust; P is the propeller power and n is the propeller rotational speed expressed in $[rev/s]$.

2.4 Wind Tunnel Corrections

2.4.1 Boundary Corrections for Propellers

The interference experienced by a propeller in a wind tunnel was object of study by Glauert [22]. A propeller, when producing a positive thrust, creates a wake or slipstream of increased velocity. Considering that in a closed wind tunnel the flow is confined between rigid walls, the condition of continuity of flow leads to reduced velocity and increased pressure of the fluid surrounding the wake. These modified conditions behind the propeller change the relationship between the thrust and the freestream velocity of the propeller for a given rotational speed.

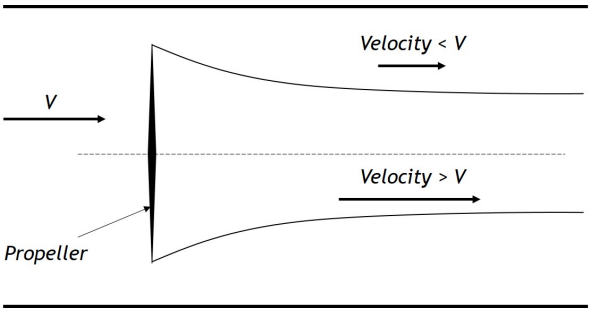

Figure 2.19: Effect of the propeller in a closed test section.

There are two different approaches to deal with this matter. In confined conditions, the thrust developed by the propeller is greater than would be developed in an unrestricted flow of the same freestream velocity with the same propeller rotation rate and blade pitch. Or, it can also be said that the thrust developed would be equal to that which would be expected at a lower U in freestream velocity [21].
The correction for this effect is:

$$\frac{U}{V} = 1 - \frac{\tau_4 \alpha_1}{2\sqrt{1 + 2\tau_4}} \quad (2.14)$$

where

$$\tau_4 = \frac{T}{\rho A V^2} \quad (2.15)$$

and

$$\alpha_1 = \frac{A}{C} \quad (2.16)$$

where A is the propeller disk area and C is the jet cross-sectional area, and T is thrust.

2.4.2 Motor Fixture Drag

Due to the presence of the torque transducer and the motor fixture, the measured thrust is actually given by $(T - D_{fixture})$. To obtain the actual values of thrust, an assembly's drag model was implemented in order to correct the measured thrust values for different freestream velocities.
The propeller thrust is, thus, given by:

$$T = \rho n^2 D^4 C_T + D_{fixture} \quad (2.17)$$

The assembly's drag can be estimated using:

$$D_{fixture} = qSC_D \quad (2.18)$$

with

$$q = \frac{1}{2}\rho V_{drag}^2 \quad (2.19)$$

Considering that the fixture is located in the propeller slipstream, a fixture drag velocity was used as the corrected freestream velocity given by Glauert's method 2.14 plus the slipstream induced velocity at the propeller disk given by the Actuator Disk Theory [23]:

$$V_{drag} = -\frac{U}{2} + \sqrt{\frac{U^2}{4} + \frac{T}{2\rho A}} + U \quad (2.20)$$

Based on the the characterization of drag coefficient of various 3D bodies [24], an approximate C_D value of 1 proved to adequate. The frontal area, $S = 0.0016m^2$, was obtained using the 3D *CAD* model (shown previously in Figure 2.11).

2.5 Balance Calibration

Before using the rig for any tests, each measuring instrument must be calibrated. The thrust calibration is made *in situ* using calibrated weights and a low-friction pulley system to create an axial load to simulate propeller thrust on the load cell. By increasing and decreasing a known force on the load cell, a linear relationship between the thrust and voltage is determined. For torque calibration, the calibrated weights are used with a moment arm to create a known torque, and by adding and removing weights, a linear relationship between the torque and voltage is calculated. These calibration procedures need to be regularly performed to ensure consistent results. The used calibration apparatus is shown in Figure 2.20.

Figure 2.20: Pictures of the thrust balance calibration procedure: (a) torque sensor (b) thrust load cell.

Calibration was later verified using check-loads. Pure and combined check-loads were repeatedly applied to verify balance calibration.

2.6 Test Methodology

For the performance tests with $J > 0$, the propeller RPM was set and the wind tunnel's freestream velocity was increased from 4 m/s to 28 m/s by 1 m/s increments. At freestream velocities smaller than 4 m/s, it was hard to obtain a stable condition to proceed with the measurements. At each measured freestream velocity, the propeller thrust and torque were measured along with the ambient pressure and temperature. If the torque value became too close to zero, the test was stopped because the propeller was entering the windmill brake state.
The collecting data procedure begins with the execution of the Labview® data acquisition and reduction software. This is followed by putting the program to run test condition. The control software powers up the motor to the first pre-defined *RPM* and data for each pre-determined velocity step is collected. This procedure was repeated for all pre-defined *RPMs*. Once the data was collected, the data reduction sub-routine is executed. The collected data is systematically reduced, recorded and archived. Due to complete automation of this process, the overall time for an entire run is just the physical tunnel run time.

2.6.1 Test Procedure

The test procedure is typically as follows:

1. Zero-load readings are recorded from the airspeed pressure transducer, the air temperature thermocouple, the thrust load cell and the torque transducer with the tunnel and propeller's motor off;

2. The propeller's motor is started and the respective motor controller sets the speed to produce the required propeller rotational speed;
3. The wind tunnel main drive motor is started and the tunnel freestream velocity is increased in 1 *m/s* increments between test points. The flow speed induced by the propeller is allowed to stabilize and, through a closed control loop, the wind tunnel motor speed is consistently held in the target freestream velocity until that test point is totally acquired. Once each freestream velocity point is acquired, the wind tunnel motor speed is increased to get another 1 *m/s* for the next point freestream velocity;
4. Once torque readings reach zero, the test is finished and the wind tunnel motor speed is slowly reduced until zero freestream velocity, where the wind tunnel motor is turned off.

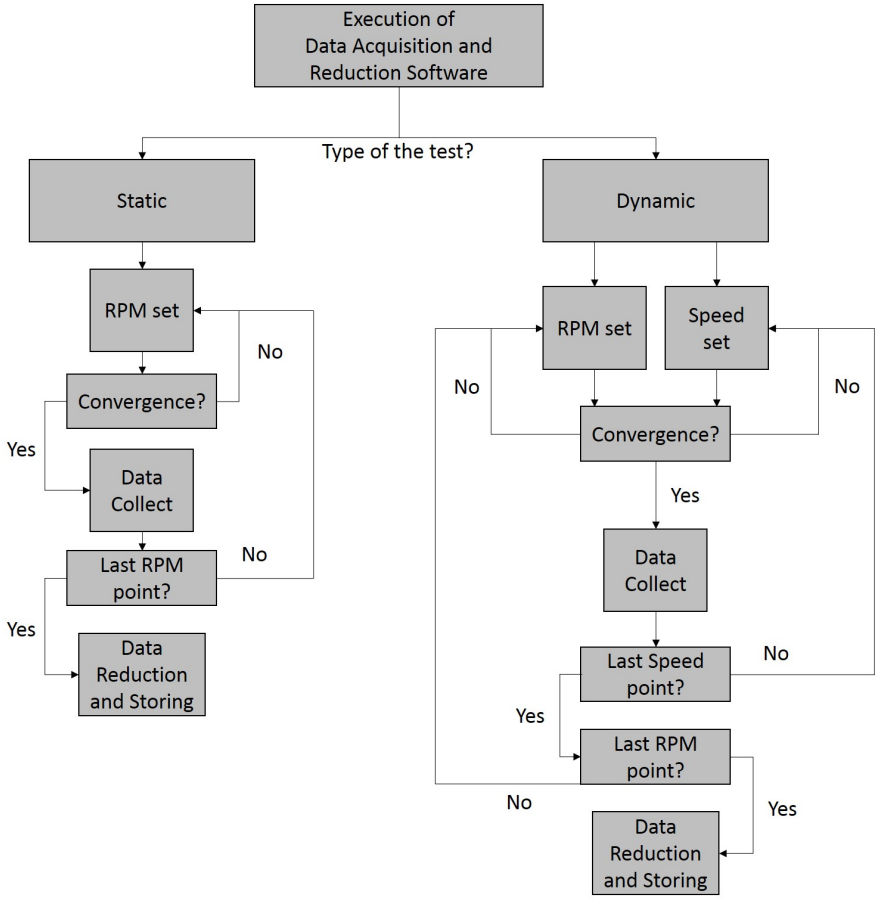

Figure 2.21: Flowchart of the test methodology.

The procedure of collecting data in each freestream velocity is preceded by a "data convergence period" to achieve the steady state. Two similar convergence criteria are implemented, one for the freestream velocity set and the other for the propeller's *RPM*. Both convergence criteria are presented in Table 2.2.

Table 2.2: Convergence criteria to achieve wind tunnel freestream speed and propeller's *RPM* steady state.

Criteria	Minimum Time [s]
$\lvert RPM - RPM_{target} \rvert \leq 10$ *RPM*	40.0
$\lvert U - U_{target} \rvert \leq 0.06$ *m/s*	40.0

When both convergence criteria are verified, the data samples are recorded over a pre-defined period of time. In Figure 2.22 an example is presented of the torque and thrust outputs during the convergence and data collect phases.

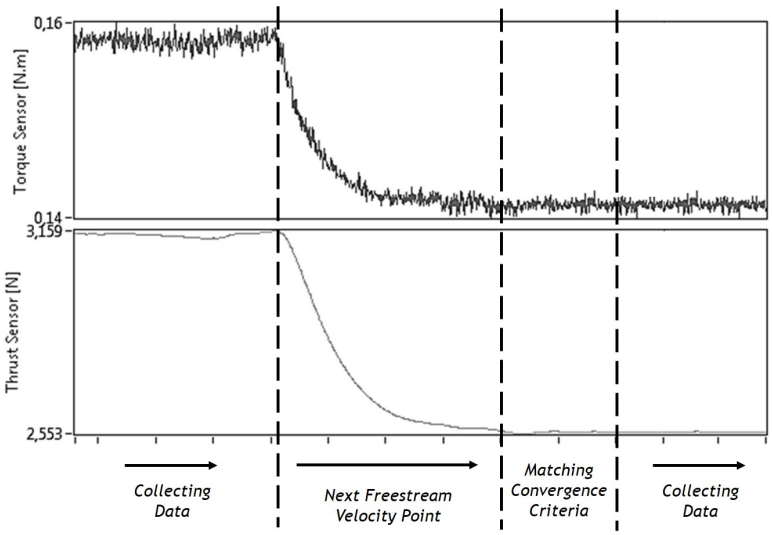

Figure 2.22: Torque and Thrust outputs during the convergence and data collection phases.

Chapter 3

Results and Discussion

3.1 System and Procedure Validation

As mentioned in Subsection 2.1.1, the test rig has been designed to afford a wide range of propellers. However, before performing any tests for new and uncatalogued propellers, the test rig was submitted to three phases of validation:

1. Sampling Independence - The same test was reproduced with five different measurement samples number settings;
2. Repeatability - The same test was performed in three distinct days;
3. Comparison - The performance of two commercial propellers was measured and compared with the performance data provided by UIUC [15] and by the manufacturer (APC).

3.1.1 Validation - Phase 1, Sampling Independence

The recorded output value of any measured or calculated variable is a mean of N samples recorded at a sampling rate of 8Hz. It is a fact that more samples reflect a more accurate result. However, as the samples number rises, the sampling time increases, so the test runtime becomes higher. This step was performed in order to find an acceptable sampling time (or sample number) that does not affect the final variable mean. In Table 3.1, five sampling settings used in this validation phase are shown. The 11x5.5" APC Thin Electric propeller was used.

Table 3.1: Sampling settings used in the first validation phase.

Number of Acquired Samples, N	**Sampling Time,** s
50	6.25
100	12.5
200	25.0
400	50.0
800	100.0

The results of this sampling setting test (see Figure 3.1), show some discrepancies for an advance ratio around 0.30 but only for the lower number of samples used to collect the data (50 and 100 samples). Additionally, it is also shown that there are no significant improvements of rising the sampling time above 25 seconds (200 samples). To ensure a correct data collection, 400 samples setting was used in all the tests presented herein, since it corresponds to a collecting phase that takes less than one minute.

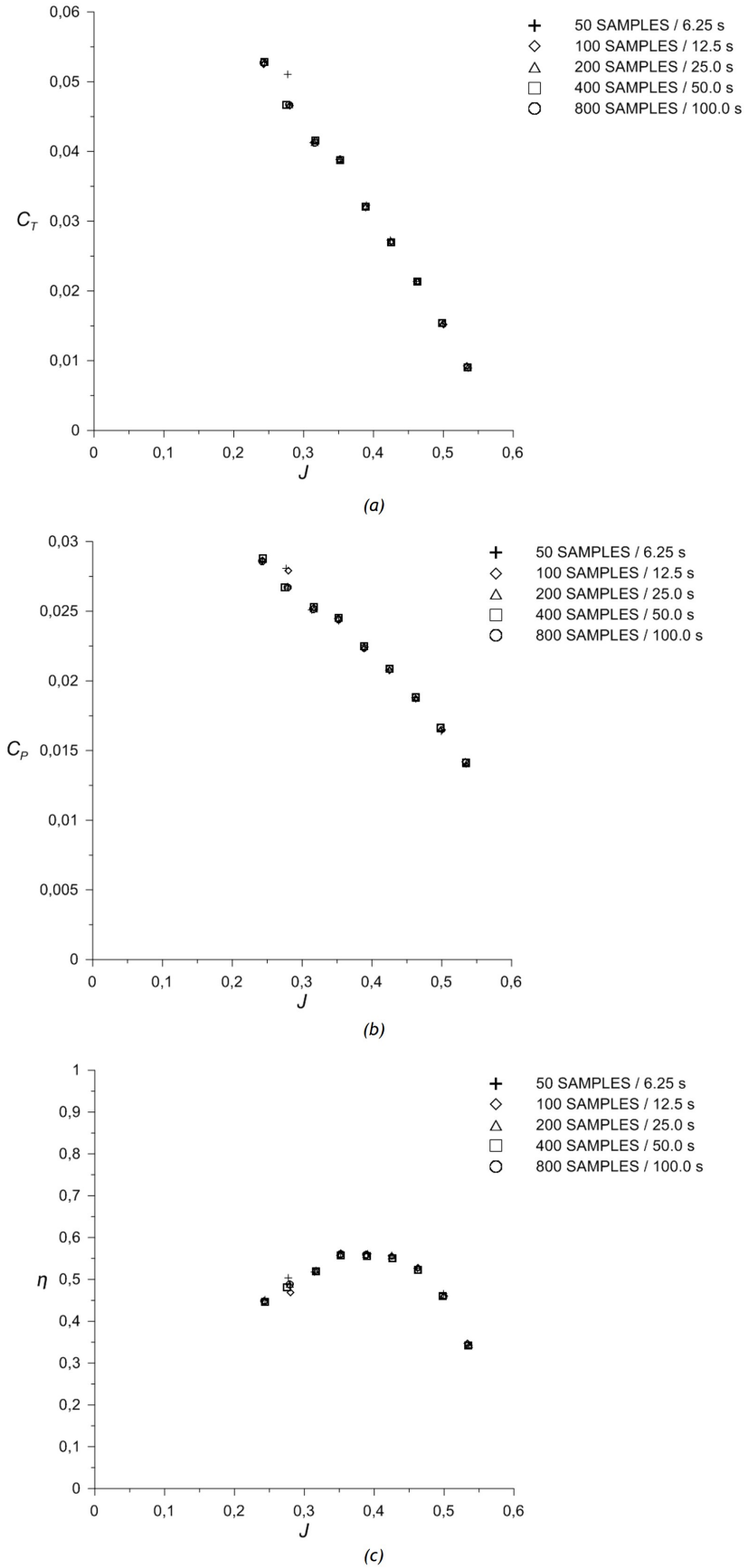

Figure 3.1: APC 11x5.5” Thin Electric Performance at 3010 *RPM* with five different sampling settings. (a) Thrust Coefficient; (b) Power Coefficient; (c) Efficiency.

3.1.2 Validation - Phase 2, Repeatability

Repeatability determines how consistent a measurement is. It can be defined by the variation in measurements taken by a single person or instrument on the same subject under the same conditions. Repeatability does not imply accuracy but it is a prerequisite for accuracy. It is an indicator of the integrity of the measurement system. If a measurement system cannot produce reliable, repeatable measurements: a verification of the measurements accuracy cannot be performed. The test rig was submitted to repeatability tests fulfilling the following conditions:

1. The same propeller;
2. The same measurement procedure;
3. The same observer;
4. The same measuring instrument, used under the same conditions;
5. The same location;
6. The same instrument calibration;
7. Repetition over 3 different days.

Figure 3.2 shows comparisons of the APC 11x5.5” Thin Electric performance measured in three different days. Although the tests were made in the Summer, the weather conditions were quite different in the three days of testing, with sun on the first test day, changing to wind and rain on the other two days of testing. However, the plotted results show that exceptional repeatability is achieved for all of the performance parameters.

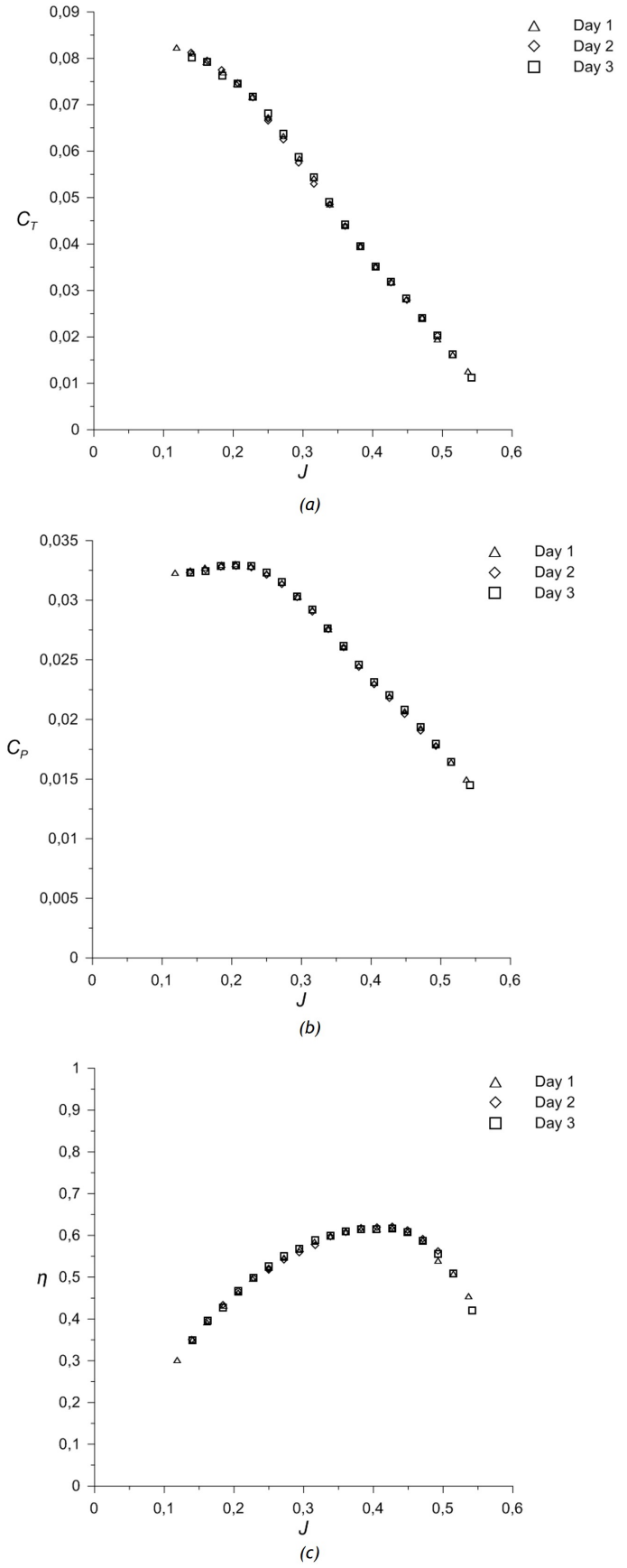

Figure 3.2: APC 11x5.5” Thin Electric Performance at 4999 *RPM* in three different days. (a) Thrust Coefficient; (b) Power Coefficient; (c) Efficiency.

3.1.3 Validation - Phase 3, Comparison with Performance Data Available in the Literature

Two different APC commercial propellers were chosen to this first step of validation, the 10x4.7" Slow Flyer and the 11x5.5" Thin Electric. Table 3.2 resumes the *RPM* settings of both non-static tests that were performed. The UIUC data, used for comparison, was downloaded from the *UIUC Propeller Database* [15] and therefore corrected using a released correction note [18]. Performance curves provided by the manufacturer (APC) are also plotted.

Table 3.2: *RPM* settings of non-static performed tests.

Propeller	RPM Tested
APC 10x4.7" Slow Flyer	4014; 4997
APC 11x5.5" Thin Electric	3010; 3994; 4999

3.1.3.1 Case 1 - APC 10x4.7" Slow Flyer Data Comparison

Figure 3.3: APC 10x4.7" Slow Flyer.

The performance data of the measurements taken on the APC 10x4.7" Slow Flyer is plotted in the charts of Figures 3.4 and 3.5, together with the results obtained by UIUC and APC. Comparing the different results, it is seen that:

1. The performance data provided by APC seem to be incorrect and will not be used in further conclusions;
2. For 4014 *RPM*, the measured C_T values are slightly lower than those of UIUC data (see Figure 3.4 (a));
3. For 4997 *RPM*, UBI's C_T data matches closely the UIUC data for $J < 0.4$, changing a slightly different slope for $J > 0.4$;
4. For both tested rotational rates (4014 and 4997), the UBI C_P values show an offset compared to UIUC data (see Figures 3.4 (b) and 3.5 (b)), with the present measurements giving a lower C_P by approx. 6%);
5. While the efficiency are very close between UBI and UIUC results for 4014 *RPM* (see Figure 3.4 (c)), for 4997 *RPM* UBI measured a maximum higher efficiency for a slightly lower advance ratio (see Figure 3.5 (c)).

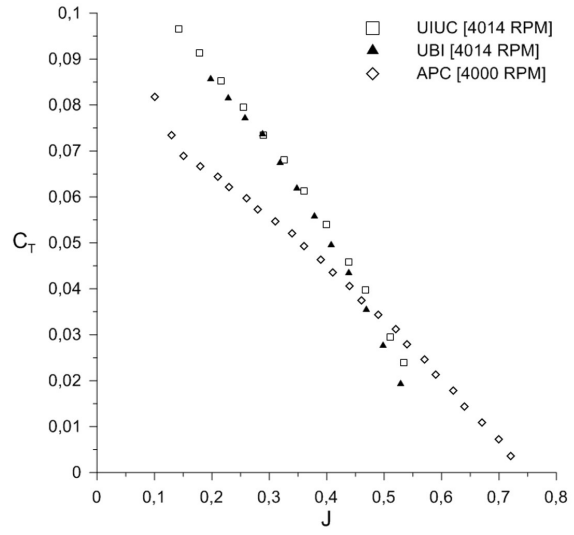

(a)

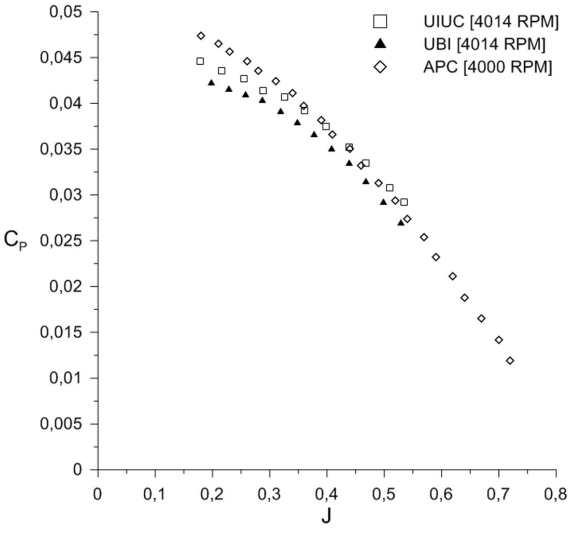

(b)

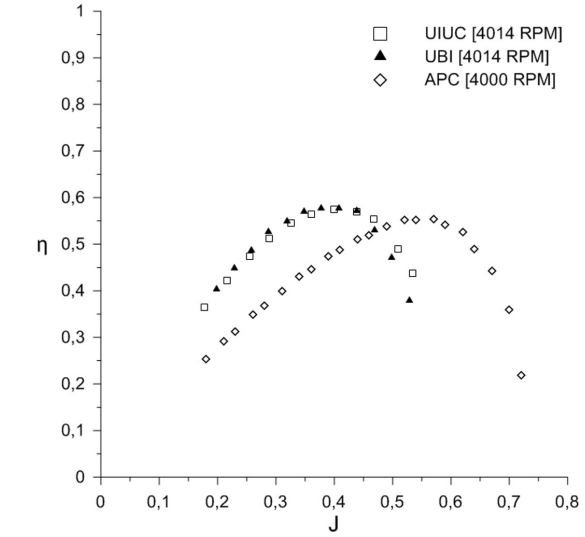

(c)

Figure 3.4: APC 10x4.7” Slow Flyer Performance at 4014 *RPM*.
(a) Thrust Coefficient; (b) Power Coefficient; (c) Efficiency.

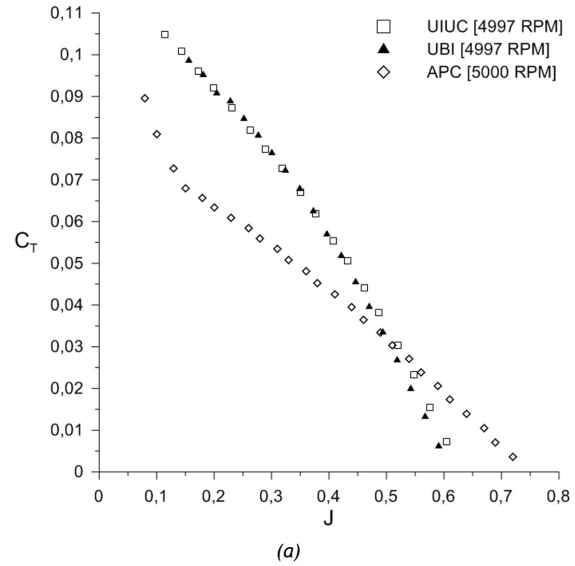

(a)

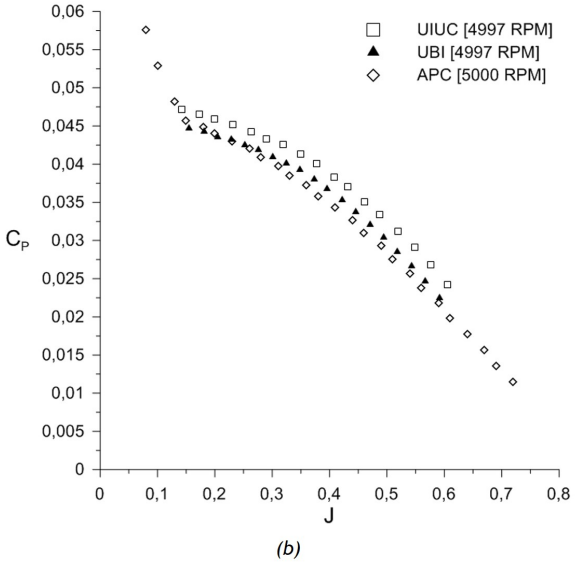

(b)

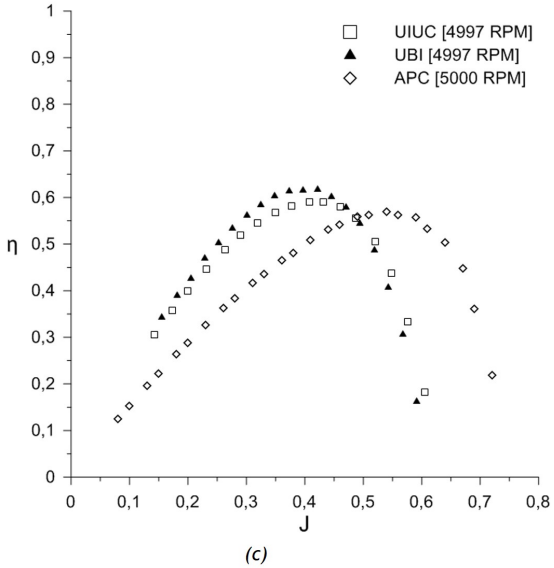

(c)

Figure 3.5: APC 10x4.7" Slow Flyer Performance at 4997 *RPM*.
(a) Thrust Coefficient; (b) Power Coefficient; (c) Efficiency.

3.1.3.2 Case 2 - APC 11x5.5" Thin Electric Data Comparison

Figure 3.6: APC 11x5.5" Thin Electric.

The performance data of the measurements taken on the APC 11x5.5" Thin Electric is plotted in the charts of Figures 3.7, 3.8 and 3.9, together with the results obtained by UIUC and APC. Comparing the different results, it is seen that:

1. The performance data provided by APC seem to be incorrect and will not be used in further conclusions;
2. For 3010 *RPM*, the measured C_T from closely matches that of UIUC (see Figure 3.7 (a));
3. For 4999 *RPM*, there is an offset on the C_T value, UBI showing a larger value. This difference is more pronounced at intermediate advance ratios (see Figure 3.9 (a));
4. Regarding the C_P, the values measured by UBI are again in good agreement for 3010 *RPM* (see Figure 3.7 (b)) and a slight difference appears at 4999 *RPM* (see Figure 3.9 (b)), with positive offset in the intermediate J values, gradually becoming negative towards the lower end of the advance ratio;
5. Since the propeller efficiency is dependent on the C_T and C_P, the differences in C_T are also present in the propeller efficiency graph.
6. In addition, it is possible to observe that both C_T and C_P increase with the increase in the propeller rotational speed. This is a typical LRN behaviour and relates to the increase of the airfoil maximum lift coefficient throughout the blade at higher Reynolds number to increased rotational speed.
7. Another airfoil characteristic that improves with the Reynolds number is the lift/drag ratio. This becomes evident observing the efficiency increase from 3010 *RPM* to 4999 *RPM*, where the UBI data shows a greater improvement than the UIUC data.

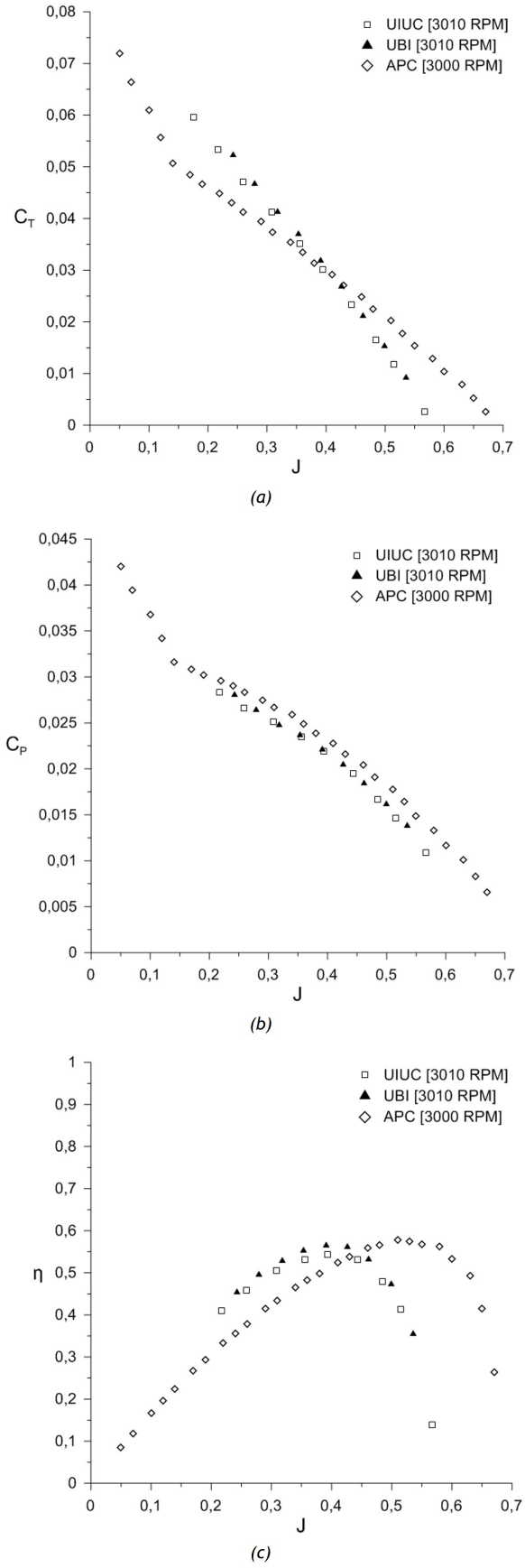

Figure 3.7: APC 11x5.5” Thin Electric Performance at 3010 *RPM*.
(a) Thrust Coefficient; (b) Power Coefficient; (c) Efficiency.

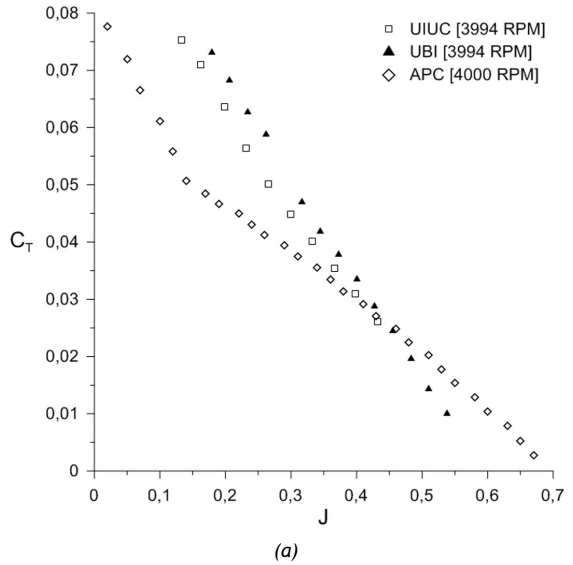

(a)

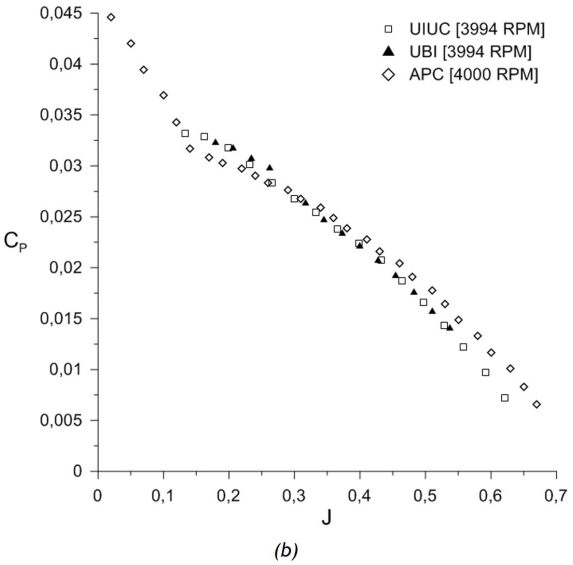

(b)

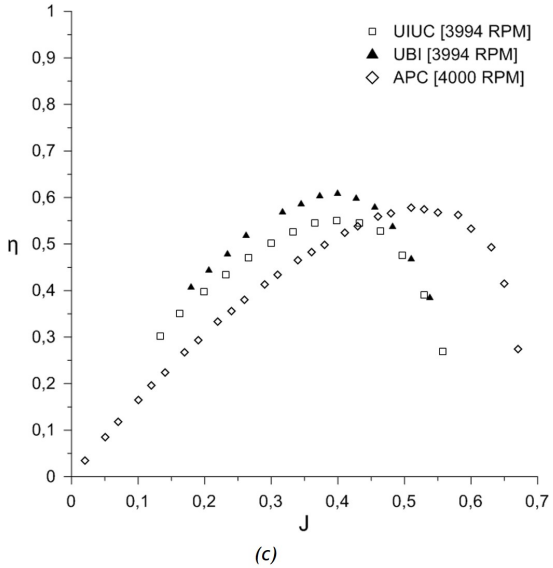

(c)

Figure 3.8: APC 11x5.5” Thin Electric Performance at 3994 *RPM*.
(a) Thrust Coefficient; (b) Power Coefficient; (c) Efficiency.

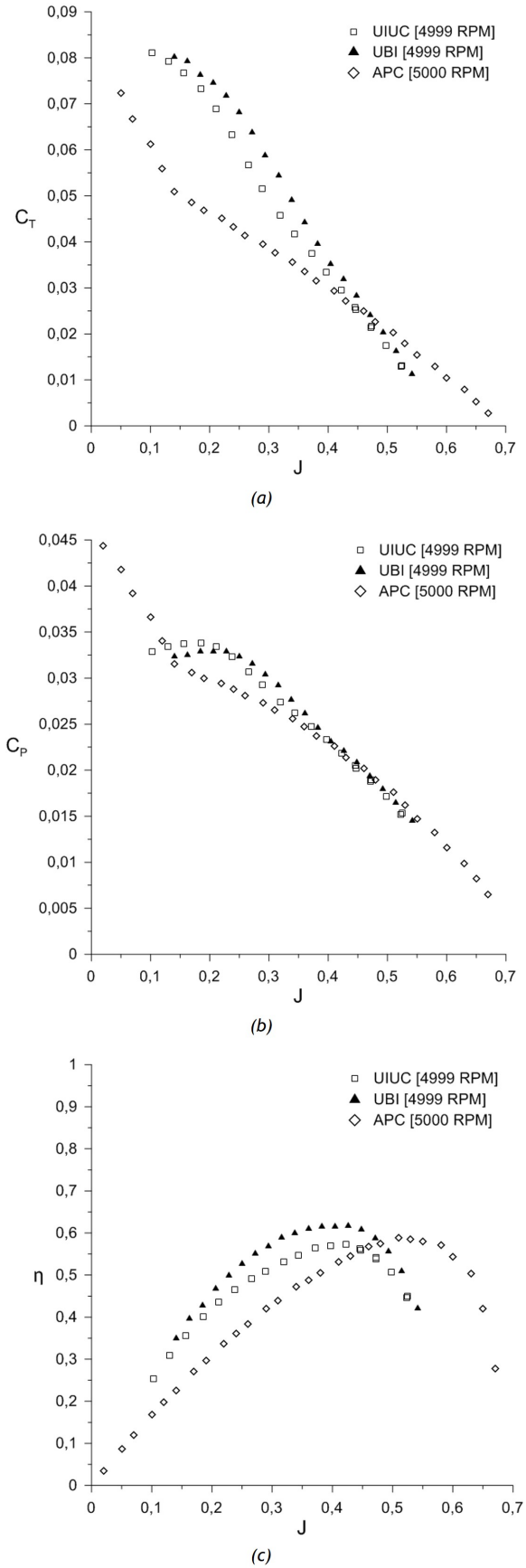

Figure 3.9: APC 11x5.5” Thin Electric Performance at 4999 *RPM*.
(a) Thrust Coefficient; (b) Power Coefficient; (c) Efficiency.

3.1.3.3 Validation Results

Regarding the differences between the obtained results and those of UIUC found in the thrust and power coefficients charts, it can be said that none of the C_T differences are systematic as they show to be positive in some cases and negative in others. One possible reason for these disparities can be one or a combination of the following factors:

1. The propeller rotational speed controlling system and the wind tunnel speed controlling mechanism used by UBI and UIUC are different causing different fluctuations on the *RPM* and freestream speed values during the measurements;

2. A different correction formulation for the motor assembly's drag, as the UBI model uses an increased slipstream velocity induced by the propeller;

3. According to Ref.[25], the individual thrust cell calibration slopes in the UIUC tests varied up to 2% over the entire test series;

During the data collecting phase (see Figure 2.22) a good rotational speed controlling mechanism seems to be critical. The average *RPM* value is not a representative number in terms of data accuracy. Considering the same average *RPM* value, the larger the fluctuation around the target *RPM*, the more power will be spent. As it stated in Ref.[25], in the UIUC tests, initially, the throttle was set manually using the knob of a device called the ServoXciter EF. After testing this *"open loop"* controlling system, it was verified that the rotational speed value floated up to $\pm$ 40 *RPM* around the target for different freestream velocities. The rotational speed controlling mechanism used by UBI is a *"closed loop"* PID controller, designed by Pedro Santos [20], showing maximum $\pm$5 *RPM* fluctuations around the target value during the data collecting phase. However, there are not sufficient data to fully assign the measured propeller performance differences to these distinct methods of controlling the propeller rotational speed.
In addition the results show that, in general, when the propeller rotational speed increases, the thrust coefficient also increases and the power coefficient slightly decreases, leading to a higher propeller efficiency for higher propeller rotational speeds.

3.2 Propeller Performance Data

Since the test rig validation process was over, the characterization of uncatalogued propellers performance started. The first tested propellers belong to two UBI's Aerospace Department in progress projects, OLHARAPO and LEEUAV. The propeller used by OLHARAPO is a 12x8" Aeronaut Carbon Electric folding 3 bladed propeller and the propeller used by LEEUAV is a 13x8" Aeronaut Carbon Electric folding 2 bladed propeller.

3.2.1 Aeronaut Carbon Electric 13x8", 2 Bladed

Results for the Aeronaut Carbon Electric 13x8" propeller in an advancing flow are shown in Figure 3.11. It is possible to observe an increase in the thrust coefficient with the Reynolds number, but no significant changes are visible in the power coefficient. Consequently, the thrust increase leads to the typical increase in the LRN propeller efficiency as the Reynolds number increases with propeller RPM as it is presented in Figure 3.11 (c).

Figure 3.10: 13x8" Aeronaut Carbon Electric, 2 bladed.

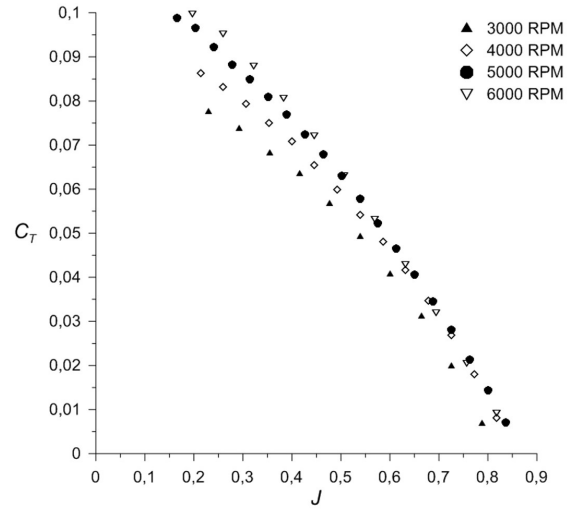

(a)

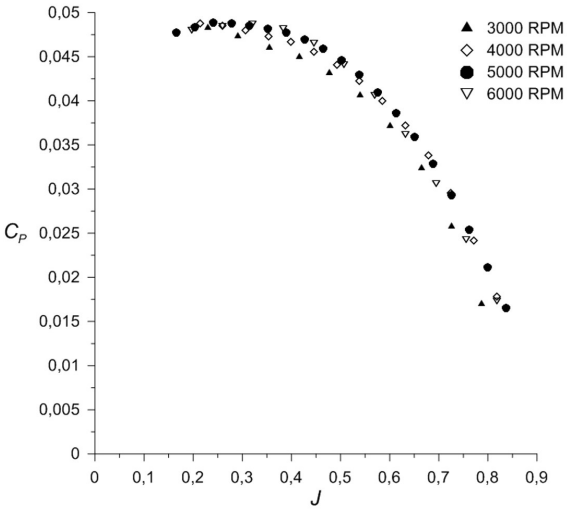

(b)

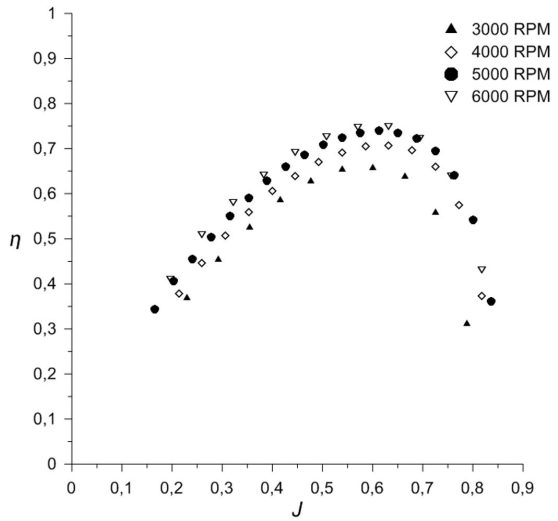

(c)

Figure 3.11: 13x8” Aeronaut Carbon Electric, 2 bladed Performance.
(a) Thrust Coefficient; (b) Power Coefficient; (c) Efficiency.

3.2.2 Aeronaut Carbon Electric 12x8”, 3 Bladed

The results of the 3 bladed Aeronaut Carbon Electric propeller are shown in Figure 3.13. Again, as commented in Subsection 3.1.3.3, it is observed an increase in both C_T and C_P with an increase in the propeller *RPM*. However, the increase in the C_T is higher than that verified in C_P. This results in a higher propeller efficiency for higher *RPM's*. The maximum efficiency of this propeller increased from about 65% for an advance ratio of 0.55 at 3000 *RPM* to 75% at a slightly higher advance ratio of 0.65 and 7000 *RPM*.

Figure 3.12: 12x8” Aeronaut Carbon Electric, 3 bladed.

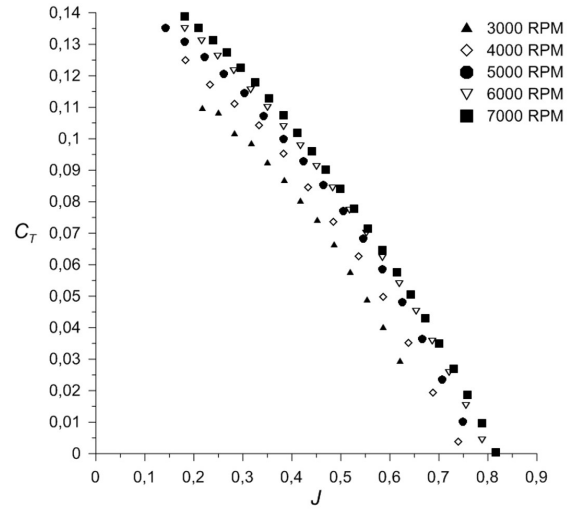

(a)

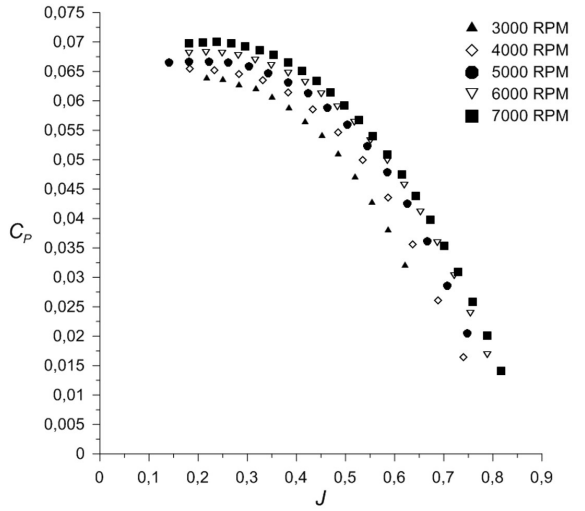

(b)

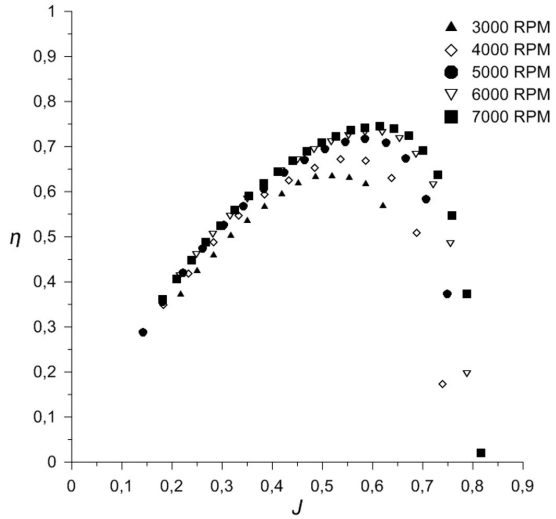

(c)

Figure 3.13: 12x8” Aeronaut Carbon Electric, 3 bladed Performance.
(a) Thrust Coefficient; (b) Power Coefficient; (c) Efficiency.

3.2.3 Propeller efficiency comparison

The four propellers subjected to the performance tests presented in this thesis, can be divided in two categories, namely the fine pitch propellers, including the two from *APC*; and the coarse pitch propellers, including the two remaining *Aeronaut* propellers. In order to investigate the effect of the propeller pitch on the overall efficiency, two additional charts are plotted in Figures 3.14 and 3.15 comparing the efficiency of the four propellers at 4000 *RPM* and 5000 *RPM* respectively.

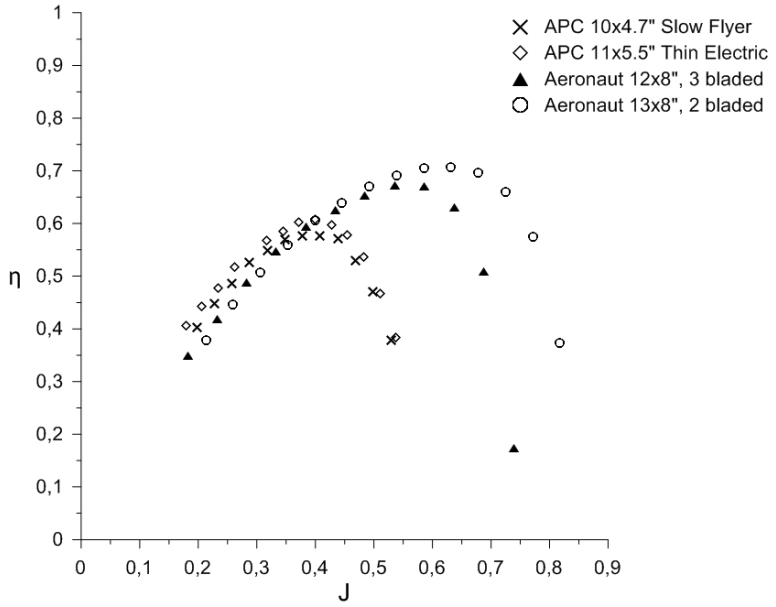

Figure 3.14: Efficiency comparison of the four tested propellers at 4000 *RPM*.

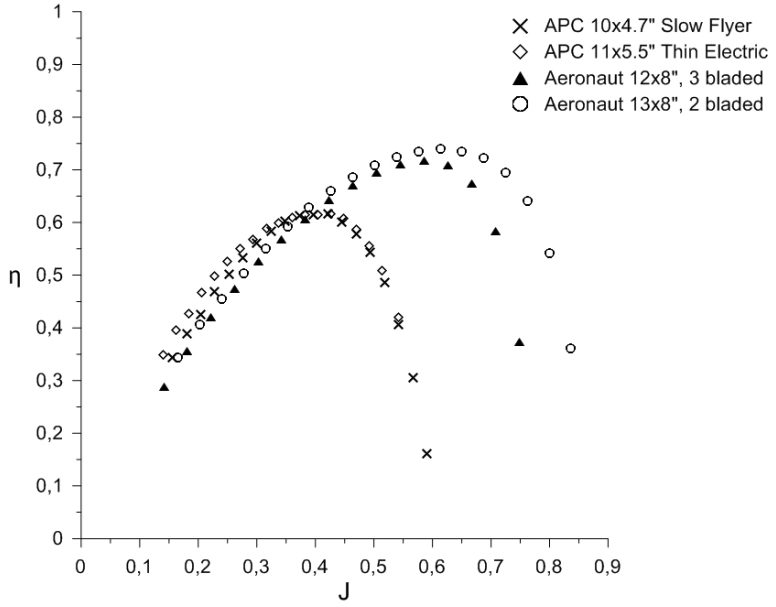

Figure 3.15: Efficiency comparison of the tested propellers at 5000 *RPM*.

Analysing the results of the comparison between the tested propellers, it is possible to observe that:

1. The two *Aeronaut* propellers, with a coarse pitch, have a higher maximum efficiency;
2. The two APC propellers shown a higher efficiency for advance ratios lower than 0.4;
3. The maximum efficiency of the tested fine pitch propellers is around 60% for an advance ratio of 0.4. On the other hand, the maximum efficiency of the *Aeronaut* propellers is about 70% for a higher advance ratio of approx. 0.6;
4. At the maximum efficiency point of the APC propellers (J=0.4), there are no significant differences in the efficiency of all the tested propellers for both rotational speeds;
5. Between both APC propellers, the APC 11x5.5" Thin Electric shows to be more efficient in all presented conditions. The difference in efficiency between this two propellers appear to be more pronounced at lower *RPM*;
6. Between both *Aeronaut* propellers, the 2 bladed *Aeronaut* 13x8" shows to be more efficient in all presented conditions. The *Aeronaut* 13x8" has a maximum efficiency of approx. 74% for an advance ratio of 0.6, while the 3 bladed *Aeronaut* 12x8" shows a maximum efficiency of approx 70% for a slightly lower advance ratio of 0.55. The difference in efficiency between this two propellers appear to be more pronounced at higher advance ratios ($J > 0.55$), this can be explained by the different number of blades;
7. The fine pitch propellers show a smaller range of usable advance ratios (0.1 to 0.6) when compared with the two coarse pitch propellers which show a wide range of operational advance ratios (0.1 to 0.85).

3.3 Uncertainty Analysis

The error propagation begins with the most basic measured quantities including thrust, torque, atmospheric pressure, temperature and flow differential pressure. The purpose of this uncertainty analysis is to determine the level of precision that the obtained values have. In order to proceed with this analysis, it is assumed that:

1. There is no error on conversion from the sensor's voltages to the physical quantities;
2. There is no error on propeller diameter since it is given as a specification from the manufacturer;
3. There is no error on the wind tunnel inner dimensions since it is given as a specification from the manufacturer.

On Table 3.3 are shown the uncertainties for each device or transducer used to collect the data.

Table 3.3: Uncertainties of the primary measurement sensors.

Measurement	Sensor	Uncertainty
Thrust, T	FGP FN3148	$\Delta T = \pm 0.05N$
Torque, Q	Transducer Techniques RTS-100	$\Delta Q = \pm 0.000339N.m$
Atmospheric Temperature, T_{atm}	National Instruments LM335	$\Delta T_{atm} = \pm 1.0K$
Atmospheric Pressure, P_{atm}	Freescale Semiconductor MPXA4115A	$\Delta P_{atm} = \pm 30.0Pa$
Propeller Rotational Speed, n	Fairchild Semiconductor QRD1114	$\Delta RPM = \pm 5RPM$
Static Ports Differential Pressure, $(p_1 - p_2)$	MKS 226A Differential Pressure Manometer	$\Delta(p_1 - p_2) = \pm(0.3\times Reading)$

The analysed uncertainties include the wind tunnel freestream velocity, the propeller advance ratio, rotational speed, coefficients of thrust and power as well as the efficiency.
The error on freestream velocity is as follow:

$$\sigma_U = \sqrt{\left[\frac{\partial U}{\partial(p_1 - p_2)}\delta(p_1 - p_2)\right]^2 + \left[\frac{\partial U}{\partial T_{atm}}\delta T_{atm}\right]^2 + \left[\frac{\partial U}{\partial P_{atm}}\delta P_{atm}\right]^2} \quad (3.1)$$

The error on advance ratio can be expressed by:

$$\sigma_J = \sqrt{\left[\frac{\partial J}{\partial(p_1 - p_2)}\delta(p_1 - p_2)\right]^2 + \left[\frac{\partial J}{\partial T_{atm}}\delta T_{atm}\right]^2 + \left[\frac{\partial J}{\partial P_{atm}}\delta P_{atm}\right]^2 + \left[\frac{\partial J}{\partial n}\delta n\right]^2} \quad (3.2)$$

The error on C_T is given by:

$$\sigma_{C_T} = \sqrt{\left[\frac{\partial C_T}{\partial T}\delta T\right]^2 + \left[\frac{\partial C_T}{\partial T_{atm}}\delta T_{atm}\right]^2 + \left[\frac{\partial C_T}{\partial P_{atm}}\delta P_{atm}\right]^2 + \left[\frac{\partial C_T}{\partial n}\delta n\right]^2} \quad (3.3)$$

The error on C_P is given by:

$$\sigma_{C_P} = \sqrt{\left[\frac{\partial C_P}{\partial Q}\delta Q\right]^2 + \left[\frac{\partial C_P}{\partial T_{atm}}\delta T_{atm}\right]^2 + \left[\frac{\partial C_P}{\partial P_{atm}}\delta P_{atm}\right]^2 + \left[\frac{\partial C_P}{\partial n}\delta n\right]^2} \quad (3.4)$$

And finally the error on efficiency is as follow:

$$\sigma_\eta = \sqrt{\left[\frac{\partial \eta}{\partial T}\delta T\right]^2 + \left[\frac{\partial \eta}{\partial Q}\delta Q\right]^2 + \left[\frac{\partial \eta}{\partial T_{atm}}\delta T_{atm}\right]^2 + \left[\frac{\partial \eta}{\partial P_{atm}}\delta P_{atm}\right]^2 + \left[\frac{\partial \eta}{\partial n}\delta n\right]^2 + \left[\frac{\partial \eta}{\partial(p_1 - p_2)}\delta(p_1 - p_2)\right]^2} \quad (3.5)$$

The partial derivatives of Eq.3.1 to 3.5 can be found in the Appendix A.1. Although the manufactures provide this uncertainty information about the sensors, all the primary readings experiment fluctuations. If the fluctuations in the measurement of parameter X are distributed normally then 95% of samples will fall within $\pm 2\sigma$ of the mean, so $\delta(X) = 2\sigma$ can be applied [26]. A summary of the uncertainty analysis relative to an CAM Carbon 12x8" Aeronaut folding, 3 bladed propeller at 5000 *RPM* test is presented on the Table 3.4. It can be noted that:

1. For freestream velocities in 5-6 m/s interval, there is an increased uncertainty. By analysing the raw data, this appears to be a result of higher fluctuations on the measurements for this freestream velocity interval;

2. For freestream velocities above 7 m/s, the uncertainty in this parameter is less than 1%;

3. The uncertainty in C_T is typically less than 0.3%;

4. The uncertainty in C_P is typically less than 0.6%;

5. The uncertainty in η is typically less than 1%.

Table 3.4: A summary of the uncertainty analysis relative to an 12x8" Aeronaut Carbon Electric folding, 3 bladed propeller at 5000 *RPM*.

	Uncertainty				
U_{target} $[m/s]$	V	J	C_T	C_P	η
4	2.834%	0.186%	0.193%	0.463%	2.874%
5	3.833%	0.178%	0.173%	0.446%	3.859%
6	2.533%	1.744%	3.363%	3.376%	3.126%
7	1.480%	0.176%	0.267%	0.502%	1.576%
8	0.817%	0.170%	0.245%	0.477%	0.964%
9	0.891%	0.166%	0.181%	0.450%	1.003%
10	0.551%	0.177%	0.222%	0.520%	0.758%
11	0.617%	0.167%	0.236%	0.468%	0.791%
12	0.420%	0.163%	0.203%	0.493%	0.660%
13	0.334%	0.166%	0.235%	0.540%	0.654%
14	0.380%	0.173%	0.332%	0.606%	0.755%
15	0.309%	0.171%	0.332%	0.654%	0.765%
16	0.376%	0.173%	0.539%	1.407%	1.533%
17	0.273%	0.171%	0.926%	0.854%	1.267%
18	0.237%	0.172%	1.290%	1.001%	1.628%

The observed uncertainties prove to be small and, as expected, they increase as the predominant primary measurement value decreases such as the uncertainty in the freestream velocity, which increases as $(p_1 - p_2)$ measurements decrease. An increased uncertainty can be found at the 5-6 m/s freestream velocity interval for all the tests. This fact suggests that, at this velocity, some type of frequency from the wind tunnel motor is affecting the measurements or the stability of the dynamic system: "test propeller - wind tunnel propeller".
The trends presented on the Table 3.4 were verified for all the studied cases. This type of analysis proved to be very helpful in detecting anomalies during the measurements allowing to reject and/or repeat any unreliable data.

Chapter 4

Conclusion

This work has presented the development and validation of a new test rig, suitable to test a wide range of LRN propellers until about 14" of diameter. The test rig was completely validated and the experimental procedure was shown herein as well. Furthermore, thrust and torque characteristics of two CAM Carbon, Aeronaut propellers were measured. It was observed that as the Reynolds number increases with the increase of propeller *RPM*, it affects the propellers performance increasing their thrust coefficient and their efficiency. The following conclusions can be drawn:

- The thrust and torque balance has been designed and built;
- The results of Propeller performance tests conducted by the UIUC have been successfully repeated, as described in Chapter 3;
- The repeatability tests show that the measuring system is highly consistent with minimal scatter in the data;
- The balance structure proved to be sound for all motor *RPM* and all freestream velocities, only showing minimal vibration for an specific condition reported in Section 3.3;
- Low uncertainty on all the measured and calculated quantities have been achieved.

The developed test rig can be used for several purposes, not only to measure a commercial propeller performance, but will also help designers improving or optimizing an existing propeller or a new design.

4.1 Future Work

Despite extensive work has been taken to fine tune the system as much as possible, to increase its data output accuracy, a few recommendations that can further improve this system are:

- Redesign the user interface of the Labview® algorithm that is being used, so it can become simpler and more intuitive;
- Produce a detailed user manual, describing the installation, calibration and operation procedures. This manual should also specify the limitations of the test rig, as well as recommendations for a safe operation;
- Design a fairing to cover the *"propeller motor-torque transducer"* set, fixing it to the existing fairing. In this way the apparatus mounting drag correction can be fully dismissed.
- Purchase a new load cell, since the one which was used already has 12 years and with a small investment, an even better one can be purchased, increasing the measurements accuracy;

- Investigate the possible usage of a motor speed controller with governor mode for an even better *RPM* control;
- Implement a cooling fan to refrigerate the motor speed controller, since high temperatures were detected during intensive use under larger current loadings;
- Find a new calibration procedure that is not influenced by the pulley friction.

Bibliography

[1] T. Theodorsen, G. W. Stickle, and M. J. Brevoort, "Characteristics of Six Propellers Including the High-Speed Range," tech. rep., NACA Technical Report No. 594, Langley, 1937. 1

[2] W. Gray, "Wind-Tunnel Tests of Two Hamilton Standard Propellers Embodying Clark Y and Naca 16-Series Blade Sections," tech. rep., NACA Technical Report No. 530, Washington, 1941. 1

[3] M. A. Silvestre, J. a. P. Morgado, and J. Pascoa, "JBLADE: a Propeller Design and Analysis Code," in *2013 International Powered Lift Conference*, (Reston), American Institute of Aeronautics and Astronautics, Aug. 2013. 1

[4] J. Morgado, M. A. R. Silvestre, and J. C. Páscoa, "Validation of New Formulations for Propeller Analysis," *Journal of Propulsion and Power*. 1

[5] M. Drela, "XFOIL: An analysis and design system for low Reynolds number airfoils," in *Low Reynolds number aerodynamics*, pp. 1–12, Springer, 1989. 1

[6] M. S. Selig and T. O. Rto, "Low Reynolds Number Airfoil Design Lecture Notes VKI Lecture Series," Tech. Rep. November, 2003. 1

[7] T. E. Markusict, J. E. Jones, and M. D. Cox, "Thrust Stand for Electric Propulsion Performance Evaluation *," pp. 1–10, 2004. 1

[8] P. T. Balance, "Construction and Performance of an Inverted Pendulum Thrust Balance," 2010. 1

[9] K. Asson, "The development of an advanced dynamometer system to experimentally determine propeller performance," 1990. 2

[10] M. P. Merchant, *Propeller Performance Measurement for Low Reynolds Number Unmanned Aerial Vehicle Applications*. PhD thesis, 2005. 2

[11] D. Rozehnal, "Measurement of the Propeller Characteristics at the Wind Tunnel," tech. rep., 2007. 2

[12] D. V. Uhlig and M. S. Selig, "Post Stall Propeller Behavior at Low Reynolds Numbers," in *46th AIAA Aerospace Sciences Meeting and Exhibit*, p. 9, 2008. 2, 3

[13] K. Tehrani, *Propellers in Yawed Flow at Low Speeds*. PhD thesis, University of Illinois, 2006. 2

[14] R. W. Deters, G. K. Ananda, and M. S. Selig, "Reynolds Number Effects on the Performance of Small-Scale Propellers," no. June, pp. 1–43, 2014. 2

[15] G. Ananda, "UIUC Propeller Database." 2, 5, 8, 23, 27

[16] K. Kotwani, S. K. Sane, H. Arya, K. Sudhakar, R. P. Minute, I. Introduction, P. Engineer, Y. P. Member, and A. Fellow, "Performance Mapping of Mini Aerial Vehicle Propellers," 3

[17] R. J. S. de Sousa, *Sistema de Hélice de Passo Variável para UAVs Elétricos*. PhD thesis, University of Beira Interior, 2012. 3, 4, 15

[18] M. S. Selig and G. Ananda, “Low Reynolds Number Propeller Perfomance Data : Wind Tunnel Corrections for Motor Fixture Drag,” no. 1, pp. 1–4, 2011. 5, 27

[19] MINITEC, “MINITEC CATALOGUE.” 9, 10

[20] P. Santos, “Pedro Santos’ Personal Notes,” tech. rep., 2012. 13, 14, 34

[21] A. Pope, J. Barlow, and W. H. Rae, *LOW-SPEED WIND TUNNEL TESTING*. 1999. 15, 18

[22] H. Glauert, *Wind Tunnel Interference on Wings, Bodies, and Airscrews*. 1933. 18

[23] W. Johnson, *Helicopter theory*. Courier Dover Publications, 2012. 19

[24] S. F. Hoerner, *Fluid-Dynamic Drag*. 1965. 19

[25] J. B. Brandt, *SMALL-SCALE PROPELLER PERFORMANCE AT LOW SPEEDS*. PhD thesis, 2005. 34

[26] W. J. Devenport and W. L. J. Hallauer, “AOE 3054 Experimental Methods Course Manual - Experimental Error,” tech. rep., A.O.E. Department, Virginia Tech. Blacksburg VA, 2006. 41

Appendix A

Appendix

A.1 Partial derivatives used on error estimation

A.1.1 Freestream velocity

$$\frac{\partial U}{\partial (p_1 - p_2)} = \frac{625 R T_{atm}}{609 P_{atm} \sqrt{\frac{1250 (p_1 - p_2) R T_{atm}}{609 P_{atm}}}} \quad \text{(A.1)}$$

$$\frac{\partial U}{\partial T_{atm}} = \frac{625 R (p_1 - p_2)}{609 P_{atm} \sqrt{\frac{1250 (p_1 - p_2) R T_{atm}}{609 P_{atm}}}} \quad \text{(A.2)}$$

$$\frac{\partial U}{\partial P_{atm}} = -\frac{625 (p_1 - p_2) R T_{atm}}{609 P_{atm}^2 \sqrt{\frac{1250 (p_1 - p_2) R T_{atm}}{609 P_{atm}}}} \quad \text{(A.3)}$$

A.1.2 Advance ratio

$$\frac{\partial J}{\partial (p_1 - p_2)} = \frac{625 R T_{atm}}{609 D P_{atm} n \sqrt{\frac{1250 (p_1 - p_2) R T_{atm}}{609 P_{atm}}}} \quad \text{(A.4)}$$

$$\frac{\partial J}{\partial T_{atm}} = \frac{625 R (p_1 - p_2)}{609 D P_{atm} n \sqrt{\frac{1250 (p_1 - p_2) R T_{atm}}{609 P_{atm}}}} \quad \text{(A.5)}$$

$$\frac{\partial J}{\partial P_{atm}} = -\frac{625 (p_1 - p_2) R T_{atm}}{609 D P_{atm}^2 n \sqrt{\frac{1250 (p_1 - p_2) R T_{atm}}{609 P_{atm}}}} \quad \text{(A.6)}$$

$$\frac{\partial J}{\partial n} = -\frac{\sqrt{\frac{1250 (p_1 - p_2) R T_{atm}}{609 P_{atm}}}}{D n^2} \quad \text{(A.7)}$$

A.1.3 Coefficient of Thrust

$$\frac{\partial C_T}{\partial T} = \frac{R T_{atm}}{D^4 P_{atm} n^2} \quad \text{(A.8)}$$

$$\frac{\partial C_T}{\partial T_{atm}} = \frac{R T}{D^4 P_{atm} n^2} \quad \text{(A.9)}$$

$$\frac{\partial C_T}{\partial P_{atm}} = -\frac{RT_{atm}T}{D^4 P_{atm}^2 n^2} \quad \text{(A.10)}$$

$$\frac{\partial C_T}{\partial n} = -\frac{2RT_{atm}T}{D^4 P_{atm} n^3} \quad \text{(A.11)}$$

A.1.4 Coefficient of Power

$$\frac{\partial C_P}{\partial Q} = \frac{2\pi RT_{atm}}{D^5 P_{atm} n^2} \quad \text{(A.12)}$$

$$\frac{\partial C_P}{\partial T_{atm}} = \frac{2\pi RQ}{D^5 P_{atm} n^2} \quad \text{(A.13)}$$

$$\frac{\partial C_P}{\partial P_{atm}} = -\frac{2\pi RT_{atm}Q}{D^5 P_{atm}^2 n^2} \quad \text{(A.14)}$$

$$\frac{\partial C_P}{\partial n} = -\frac{4\pi RT_{atm}Q}{D^5 P_{atm} n^3} \quad \text{(A.15)}$$

A.1.5 Efficiency

$$\frac{\partial \eta}{\partial T} = \frac{\sqrt{\frac{1250(p_1-p_2)RT_{atm}}{609P_{atm}}}}{2\pi Qn} \quad \text{(A.16)}$$

$$\frac{\partial \eta}{\partial Q} = -\frac{T\sqrt{\frac{1250(p_1-p_2)RT_{atm}}{609P_{atm}}}}{2\pi Q^2 n} \quad \text{(A.17)}$$

$$\frac{\partial \eta}{\partial (p_1-p_2)} = \frac{625RT_{atm}T}{1218\pi P_{atm}Qn\sqrt{\frac{1250(p_1-p_2)RT_{atm}}{609P_{atm}}}} \quad \text{(A.18)}$$

$$\frac{\partial \eta}{\partial T_{atm}} = \frac{625R(p_1-p_2)T}{1218\pi P_{atm}Qn\sqrt{\frac{1250(p_1-p_2)RT_{atm}}{609P_{atm}}}} \quad \text{(A.19)}$$

$$\frac{\partial \eta}{\partial P_{atm}} = -\frac{625RP_{atm}(p_1-p_2)T}{1218\pi P_{atm}^2 Qn\sqrt{\frac{1250(p_1-p_2)RT_{atm}}{609P_{atm}}}} \quad \text{(A.20)}$$

$$\frac{\partial \eta}{\partial n} = -\frac{T\sqrt{\frac{1250(p_1-p_2)RT_{atm}}{609P_{atm}}}}{2\pi Qn^2} \quad \text{(A.21)}$$

Low Reynolds Number Propeller Performance Testing

MIGUEL SILVESTRE, JOÃO MORGADO, PEDRO ALVES, PEDRO SANTOS
PEDRO GAMBOA, JOSÉ PÁSCOA
Faculty of Engineering
University of Beira Interior (UBI)
R Calçada Fonte do Lameiro, Edifício II das Engenharias, 6200-358 Covilhã
PORTUGAL
mars@ubi.pt https://www.ubi.pt/Pagina_Pessoal.aspx?id=mars

Abstract: - This paper reports the efforts of characterizing the performance of low Reynolds number propellers. Propellers are efficient propulsion devices for low velocity aerial vehicles. In low Reynolds numbers applications such as the case of high altitude airships' propulsion, their aerodynamics design is not straightforward. In order to adequately develop and validate numerical design tools for these devices, accurate experimental data is needed. The development of an experimental setup for propeller testing is herein described. The measurements of that test rig are validated against reference data and additional performance data is given for propellers that are not characterized in the existing literature.

Key-Words: - Low Reynolds, Propellers, Wind Tunnel, Experiments, Airships, MAAT project

1 Introduction

In the last years, high-altitude airships have been considered as a platform for different purposes [1]. Particularly, for application as telecommunication platforms, surveillance, monitoring and for transportation of people and goods [2–7]. In Europe, the Multibody Concept for Advanced Airship for Transport (MAAT [8]) airships are being developed as an alternative medium and long range transportation system. The project involves 12 different institutions and aims to develop a heavy lift cruiser–feeder airship system. Since the cruiser will operate at stratospheric altitudes, propellers are a valid option for propulsion [6,9–15].

Due to the high altitudes the MAAT airship propellers will operate in a Low Reynolds Number (LRN) flow environment. LRN effects can decrease the performance of propellers and the ability of the available numerical methods to predict that performance. To deal with this, JBLADE [16] software is being developed, as an open-source propeller design code, using a modified [17] Blade Element Momentum (BEM) theory which accounts for three dimensional flow equilibrium. The software is coupled with [18] for its suitability in predicting LRN airfoil performance [19] JBLADE will be used to design different propellers as well as to estimate their off-design performance.

To improve the prediction capability of JBLADE, accurate LRN propeller performance data is needed.

Experimental work on propeller performance was abundant before WWII [20,21] and a sound database of propeller performance characteristics got established. That was the golden age of propeller driven aircraft. After WWII, the widespread of jet propulsion limited the use of propellers to light aircraft. However, in recent times, the small Unmanned Aerial Vehicles (UAV) advent has triggered the interest in the LRN wing and propeller aerodynamics. UIUC Applied Aerodynamics Group is a world leading institution, very active in the study of LRN aerofoils and propellers, with several publications describing experimental studies on propeller performance [22–24].

This paper describes the development of a test rig for measuring propeller performance and the experimental tests procedure simulating the LRN environment found at high altitudes. A number of wind tunnel tests performed on different small propellers is reported. In addition, the validation of the experiments is described in detail and performance data not found in the literature is presented for a couple of well-known commercial propellers.

2 Methodology

2.1 Experimental Setup

The design chosen for the propeller thrust balance closely resembles the T-shaped pendulum concept implemented by UIUC [22]. A sketch of the design is

shown in Fig. 1. An effort was made to reduce the complexity of the assembly inside the wind tunnel, in order to ensure minimal flow and measuring disturbances. The T-shaped pendulum is pivoted about two flexural pivots while being constrained by a load cell outside of the tunnel in an area above the test volume, where plenty of room is available. The flexural pivots are frictionless, stiction-free bearings with negligible hysteresis that are suited for applications with limited angular travel. The pivots are made with flat, crossed flat springs that support rotating sleeves. These flexural pivots were chosen over the standard bearings since they greatly reduce the adverse tendencies that bearings are prone to, when used in static applications, namely stiction and hysteresis.

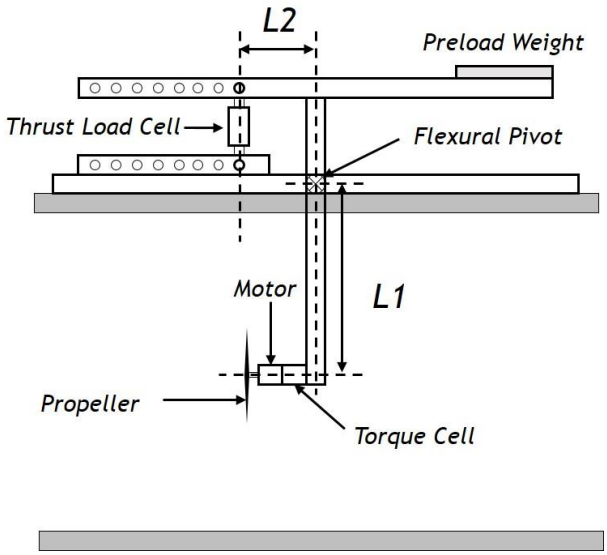

Fig. 1 - T-shaped pendulum thrust balance concept.

The pendulum was designed in order to have the thrust vector located at the center of the test section. Another design concern was to ensure that there would be enough space for assembling the load cell and its accessories above the wind tunnel upper wall. Due to the 0.8m×0.8m dimensions of the test cross-section, it was decided to limit the maximum diameter of the propellers that can be tested to 14". Using the data available at the propeller performance database provided by UIUC [25], it was concluded that for 14" propellers, in static conditions, the worst case scenario, the maximum measured thrust is close to 15N.

A preload weight was added to the balance on the opposite side to the load cell (see Fig. 2). This preload weight keeps the load cell in tension throughout propeller testing to make sure the load cell does not slip during negative thrust conditions.

2.1.1 Load Cell Variable Positioning

One of the key concepts for the assembly's sensitivity is the possibility to adjust the position of the load cell along the upper arm of the pendulum. Thus, it becomes possible to use the full range of the load cell for different intervals of propeller's produced thrust. Fig. 2 shows the system sketch, such that the distance *L2* can be adjusted between 80*mm* and 350*mm* in 10 increments of 30*mm* each.

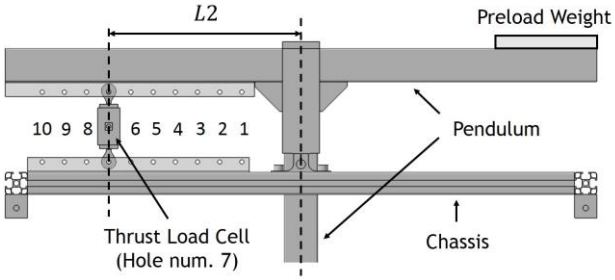

Fig. 2 – Illustration of different load cell positions.

2.1.2 Thrust and Torque Measurement

The thrust load cell used is the FN3148 manufactured by *FGP Sensors & Instrumentation* having a maximum capacity of 100N. The torque produced by the propeller is measured using the RTS-100 and RTS-200 reaction torque transducers made by Transducer Techniques according to the torque level of the propeller being tested. Both thrust and torque load cells are connected to a high-precision strain gauge converter from *mantracourt*, model SCB-68 that converts a strain gauge sensor input to a digital serial output.

2.1.3 Propeller Speed Measurement

To measure the propeller rotation speed, a Fairchild Semiconductor QRD1114 photo-reflector was used to count the number of revolutions the output shaft makes in a fixed time interval (0.75*s*), resulting on an accuracy of ±0.5*Rev*/0.75*s*. This sensor is constituted by two distinct parts: an infrared emitting diode and a phototransistor. A simple circuit composed by a limiting resistor, a bias resistor and a *Schmitt trigger* is used. The former is used, as the name suggests, to limit the current to the infrared diode. The bias resistor is used to produce an output on the phototransistor side. The output of the phototransistor is further cleaned and digitized using a *Schmitt trigger*. The latter component is essential in order to make the output relatively independent of the distance from the reflecting surface.

Using this circuit, the sensor can be placed up to 2*mm* away from the reflective surface. The output voltage is near 0.27*V* when aimed at a white surface and about 4.61*V* when pointed at a black surface. The circuit has a response time of around 50μs. The output voltages and response time of the circuit proved to be more than sufficient for measuring the rotational speed of the propellers, which never exceeded 7000 *RPM* as shown in Section 3.

2.1.4 Freestream Velocity Measurement

The freestream velocity is measured with a differential pressure transducer, an absolute pressure transducer, and a thermocouple. The measuring mechanism uses two static pressure ports, one at the tunnel settling section and another at the entrance of the test volume, as it presented in Fig. 3.

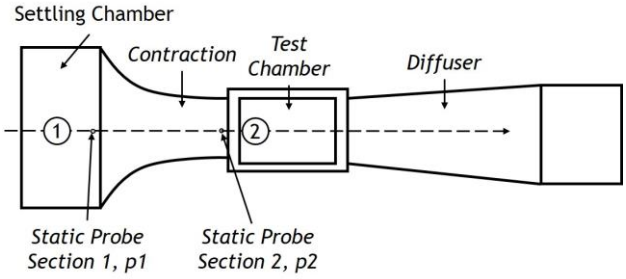

Fig. 3 – Location of the static pressure ports.

The contraction section makes the velocity increase and the pressure decrease at the test chamber. This pressure difference is a measure of the tunnel flow rate. Thus, the velocity can be determined from Bernoulli's equation:

$$\frac{p_1}{\rho}+\frac{1}{2}V_1^2+gz_1=\frac{p_2}{\rho}+\frac{1}{2}V_2^2+gz_2 \qquad (1)$$

Considering that the tunnel is horizontal, $z_1=z_2$, then:

$$V_2^2-V_1^2=\frac{2(p_1-p_2)}{\rho} \qquad (2)$$

The incompressible continuity relationship:

$$A_1V_1=A_2V_2 \qquad (3)$$

or

$$V_1=\frac{A_2}{A_1}V_2 \qquad (4)$$

Combining (2) and (4), allows the determination of the flow velocity in the test section:

$$V_2=\sqrt{\frac{2(p_1-p_2)}{\rho\left[1-\left(\frac{A_2}{A_1}\right)^2\right]}} \qquad (5)$$

The atmospheric pressure outside of the tunnel is measured with the absolute pressure transducer model MPXA4115A made by Freescale Semiconductor. The temperature is measured with a National Instruments LM335 thermocouple located at the inlet of the wind tunnel. This measuring method is also independent of possible inaccurate installations regarding the correct direction of the pitot probe as it uses the factory pre-installed wind tunnel static pressure ports.

2.2 Balance Calibration

Before using the rig for any tests, each measuring instrument was calibrated. The thrust calibration was made *in situ* using calibrated weights and a low-friction pulley system to create an axial load simulating the propeller thrust on the load cell. By increasing and decreasing a known force on the load cell, a linear relationship between the thrust and voltage was determined. Regarding torque sensor calibration, the calibrated weights are used with a moment arm to create a known torque, and by adding and removing weights, a linear relationship between the torque and voltage was also calculated. These calibration procedures need to be regularly performed to ensure consistent results. Calibration was later verified using check-loads. Pure and combined check-loads were repeatedly applied to verify the balance calibration.

(a) (b)

Fig. 4 – Pictures of the thrust balance calibration procedure: (a) torque sensor (b) thrust load cell

2.3 Propeller Performance Parameters

Variables can be divided into two categories, namely measured and calculated variables. The measured variables are directly obtained from the measurement instruments. Physical measurements of thrust, torque, rotational speed, static pressures, atmospheric pressure, and temperature are gathered. From these quantities, propeller power and air density are calculated, respectively, according to:

$$P=2\pi nQ \qquad (6)$$

$$\rho = \frac{P_{abs}}{RT_{atm}} \quad (7)$$

The above measured and derived quantities are non dimensionalized in order to obtain the propeller performance characteristics. These quantities include the thrust coefficient C_T, power coefficient, C_P, and propeller efficiency, η. In the static case, since the advance ratio is zero, C_T and C_P are plotted against the propeller rotational speed. For the non-static case, the coefficients and the efficiency are plotted against the advance ratio. The definitions for the advance ratio, thrust and power coefficients, and propeller efficiency are, respectively, given by:

$$J = \frac{V}{nD} \quad (8)$$

$$C_T = \frac{T}{\rho n^2 D^4} \quad (9)$$

$$C_P = \frac{P}{\rho n^3 D^5} \quad (10)$$

$$\eta = J\frac{C_T}{C_P} \quad (11)$$

where, V is the freestream velocity; D is the propeller diameter; T is the propeller thrust; P is the propeller power and n is the propeller rotational speed expressed in *rot/s*.

2.4 Wind Tunnel Corrections

2.4.1 Boundary Corrections for Propellers

The interference experienced by a propeller in a wind tunnel was object of study by Glauert [26]. A propeller, when producing a positive thrust, creates a wake or slipstream of increased velocity. Considering that in a closed wind tunnel the flow is confined between solid walls, the condition of flow continuity leads to reduced velocity and increased pressure of the fluid surrounding the wake.

These modified conditions behind the propeller change the relationship between the thrust and the freestream velocity of the wind tunnel propeller for a given rotational speed. Such that, in confined conditions, the thrust developed by the propeller is greater than would be developed in an unrestricted flow of the same freestream velocity with the same propeller rotation rate and blade pitch. Or, it can also be said that the thrust developed would be equal to that which would be expected at a lower V' in freestream velocity [27]. The correction for this effect is:

$$\frac{V'}{V} = 1 - \frac{\tau_4 \alpha_1}{2\sqrt{1+2\tau_4}} \quad (12)$$

where

$$\tau_4 = \frac{T}{\rho A V^2} \quad (13)$$

and

$$\alpha_1 = \frac{A}{C} \quad (14)$$

where A is the propeller disk area and C is the jet cross-sectional area, and T is thrust.

2.4.2 Motor Fixture Drag

Due to the presence of the torque transducer and the motor fixture, the measured thrust is actually given by (T-$D_{fixture}$). To obtain the actual values of thrust, an assembly's drag model was implemented in order to correct the measured thrust values for different freestream velocities. The propeller thrust is, thus, given by:

$$T = \rho n^2 D^4 C_T + D_{fixture} \quad (12)$$

The assembly's drag is estimated using:

$$D_{fixture} = qSC_D \quad (13)$$

With,

$$q = \frac{1}{2}\rho V_{drag}^2 \quad (14)$$

Considering that the fixture is located in the propeller slipstream, a fixture drag velocity was used as the corrected freestream velocity given by Glauert's method 2.14 plus the slipstream induced velocity, at the propeller disk, given by the Actuator Disk Theory.

$$V_{drag} = -\frac{V'}{2} + \sqrt{\left(\frac{V'}{2}\right)^2 + \frac{T}{2\rho A}} + V' \quad (15)$$

2.5 Test Methodology

For static performance tests, the propeller thrust and torque were measured along with the local atmospheric pressure and temperature at different RPM. For the performance tests with freestream speed, the propeller rotational speed was set to a desired value and the wind tunnel's freestream velocity was increased from 4 *m/s* to 28 *m/s* by 1 *m/s* increments. At freestream velocities smaller than 4 *m/s*, it was difficult to obtain the needed freestream velocity stability to proceed with the measurements,

due to the interference between the propeller wake and the wind tunnel's fan. At each measured freestream velocity, the propeller thrust and torque were measured along with the ambient pressure and temperature. If the torque value became too close to zero, the test was finished because the propeller was entering the windmill brake state.

The collecting data procedure begins with the execution of the LabView® data acquisition and reduction software. This is followed by putting the program to run test condition. The control software powers up the motor to the first pre-defined RPM setting and data for each freestream velocity step is collected. This procedure was repeated for all $RPMs$. Once the data was collected, the data reduction sub-routine is executed. The collected data is systematically reduced, recorded and stored. Due to the complete automation of the process, the overall time for an entire run is just the physical tunnel run time. The procedure of collecting data in each freestream velocity is preceded by a "data convergence period" of 60s within a minimum error margin from the intended defined RPM and freetream velocity values to achieve the steady state.

3 Validation of the Test Rig

Before performing tests for new and uncatalogued propellers, the test rig was submitted to a complete validation study. The validation included a sample independence test in order to ensure that the results are not affected by the number of samples used to collect each point. The same propeller test was run with five different sampling settings as presented in Section 3.1. In addition, to ensure the repeatability of the measurements, the same propeller was tested in 3 different days, as shown in Section 3.2. Furthermore, the propeller performance obtained in UBI's wind tunnel was compared with the data obtained by UIUC[28].

3.1 Sampling Independence

The recorded output value of any measured or calculated variable is a mean of *N* values recorded at a sample rate of 8*Hz*. Since this frequency is constant, when the sample number, N, increases, the sampling time also increases and the test runtime becomes higher. This validation test was performed in order to find an acceptable samples number that does not affect the final result. The APC 11"x5.5" Thin Electric propeller was used. The results, presented in Fig. 5 show some discrepancies for an advance ratio around 0.3 for the lower number of samples used to collect the data (50 and 100 samples) but converge for $N > 200$. To ensure a correct data collection, 400 samples setting was used in all the tests presented herein. That with the 8 *Hz* sampling rate made each point collecting phase takes less than one minute.

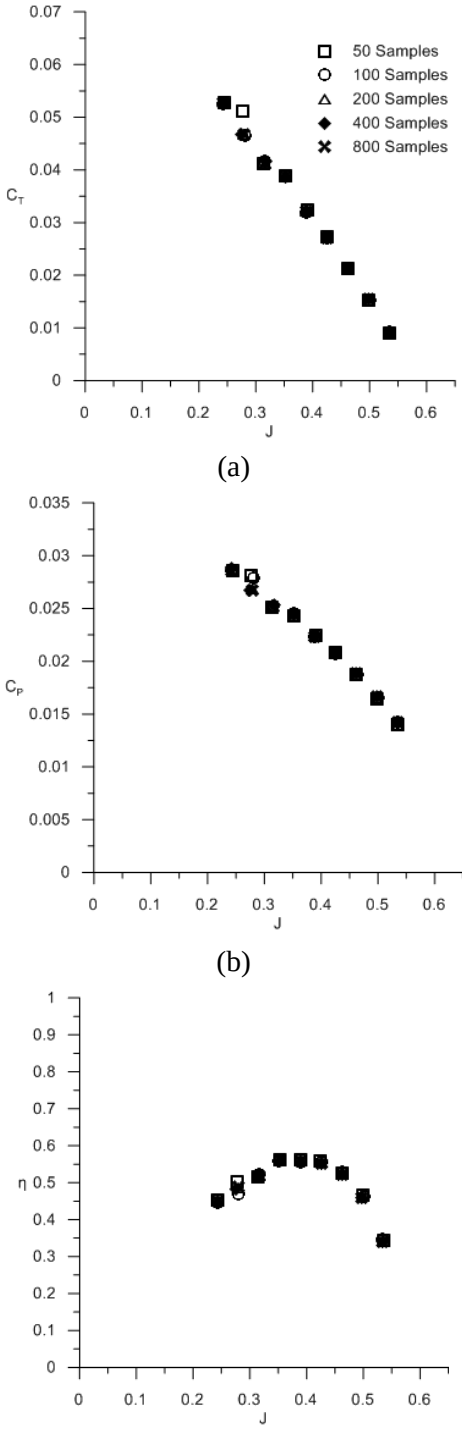

Fig. 5 – Comparison using different number of samples for an APC 11"x5.5". (a) thrust coefficient (b) power coefficient (c) propeller efficiency

3.2 Measurements Repeatability

To ensure that the measurements are not dependent on the weather conditions on a specific day, the measurements for a specific propeller were performed on 3 distinct days. Furthermore, the measurements repeatability quality is an indicator of the integrity of the measurement system. If a measurement system cannot produce consistent and repeatable measurements, a verification of the measurements accuracy cannot be performed. The test rig was submitted to repeatability tests fulfilling the following conditions:

- The same propeller and the same measurement procedure;
- The same measuring instruments, used under the same conditions;
- The same instrument calibration;
- Repetition over 3 consecutive days.

Fig. 6 shows comparisons of the APC 11”x5.5” Thin Electric performance data collected for the repeatability tests. Although the tests were performed during the summer, the weather conditions were quite different in the three days of testing, with sun on the first day moving to wind and rain on the remaining two days. However, the plotted results show an exceptional repeatability for all the performance parameters.

3.3 Performance Data Comparison

An APC commercial propeller was used, the APC 11”x5.5” Thin Electric and its performance data was compared with data available in the literature. The data for comparison was downloaded from the UIUC Propeller Data Site [25] and corrected according to Ref. [29].

Analyzing the results of the APC 11”x5.5” Thin Electric propeller (see Fig. 7), it is possible to observe that for 3000*RPM*, the thrust coefficient from closely matches that of UIUC [25]. On the other hand, for 5000*RPM* there is an offset on the thrust coefficient value, UBI showing a larger value. This difference is more pronounced at intermediate advance ratios. Regarding the power coefficient, the values measured by UBI are again in good agreement for 3000*RPM* and a slight difference appears at 5000 *RPM*, with positive offset in the intermediate *J* values, gradually becoming negative towards the lower end of the advance ratio. Since the propeller efficiency is dependent on the thrust and power coefficients, the differences in thrust coefficients are also present in the propeller efficiency graph. In addition, it is possible to observe that both thrust and power coefficients increase with the increase in the propeller rotational speed. This is a typical LRN behavior and relates to the increase of the airfoil maximum lift coefficient throughout the blade at higher Reynolds number to increased rotational speed. Another airfoil characteristic that improves with the Reynolds number is the lift/drag ratio. This becomes evident observing the efficiency increase from 3000*RPM* to 5000*RPM*, where the UBI data shows a greater improvement than the UIUC data. Nevertheless, the curve trends that are a clear feature of the propeller model are alike.

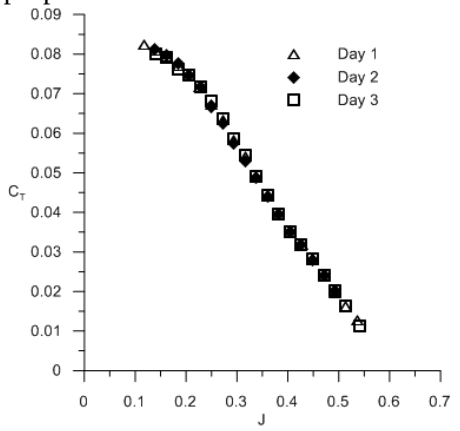

(a)

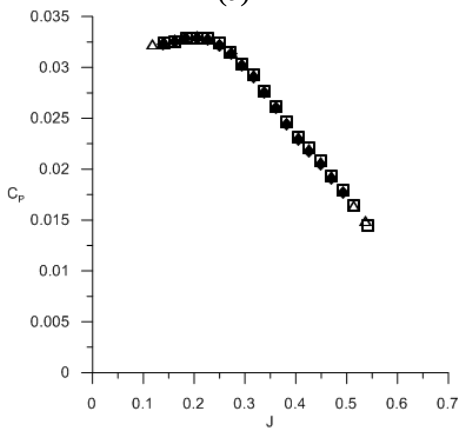

(b)

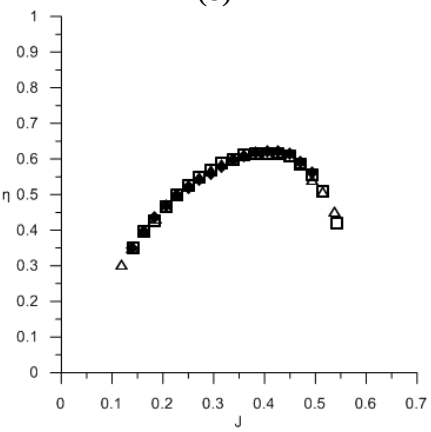

(c)

Fig. 6 – Comparison of measurements performed in 3 different days. (a) thrust coefficient (b) power coefficient (c) propeller efficiency

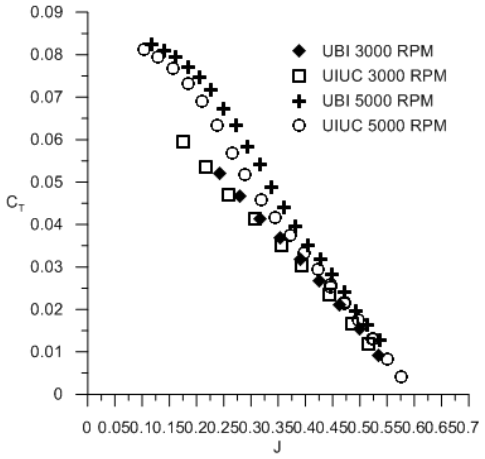

(a)

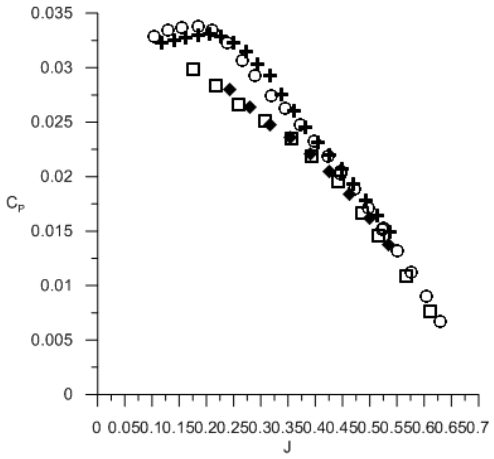

(b)

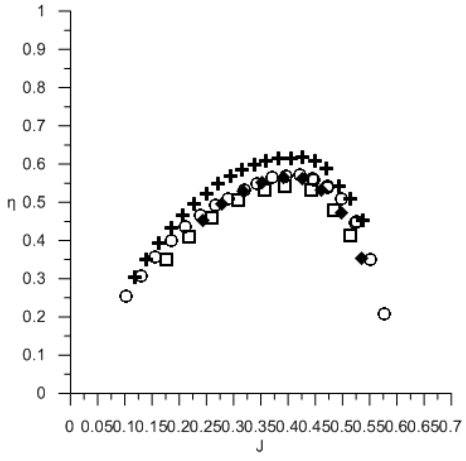

(c)

Fig. 7 – APC 11”x5.5” Propeller data for 3000 *RPM* and 5000 *RPM* (a) thrust coefficient (b) power coefficient (c) propeller efficiency

The existing differences in the performance between UBI and UIUC data can be explained by the different propeller rotational speed controlling system used by UBI and UIUC. During the collecting data phase an effective rotational speed control mechanism is a key factor. There is a large coupling between the wind tunnel freestream velocity and the propeller rotational speed. So, the average propeller rotational speed value is not a representative number in terms of data accuracy in case there is significant *RPM* variance, σ. Considering the same average *RPM* value, the higher the fluctuations around the target *RPM*, the higher the power that will be consumed. As it is stated in Ref. [28], UIUC initially used a manual control of the throttle setting through the knob of a device called the ServoXciter EF. After testing this “open loop” controlling system it was observed the actual *RPM* values fluctuated up to 40 *RPM* around the target value for different freestream velocities. UBI uses a closed loop PID controller, showing maximum fluctuations of 5 *RPM* around the target *RPM* value during the data collection.

3.4 Propeller Performance Data

After validating the test rig, two uncatalogued propellers were tested. These propellers belong to two different UBI's Aerospace Science Department UAV projects: OLHARAPO and LEEUAV. The propeller used by OLHARAPO is a 12”x8” Aeronaut CAM Carbon Electric folding, with 3 blades. Regarding the LEEUAV, it uses a 13”x8” Aeronaut CAM Carbon Electric folding, 2-bladed propeller.

3.4.1 Aeronaut CAM Carbon Electric 12”x8” – 3 Blades

The results of the 3 bladed Aeronaut CAM Carbon Electric propeller are shown in Fig. 8. The results show an increase in both thrust coefficient and power coefficient with an increase in the propeller *RPM*. However, since the increase in the thrust coefficient is higher than that of the power coefficient, it results in a higher propeller efficiency for higher *RPM's*. As mentioned in Section 3.3 this is due LRN detrimental effect fading away as the Reynolds number increases with the rotational speed.

The maximum efficiency of this propeller increases from about 65% for an advance ratio of 0.55 at 3000 *RPM* to 75% at an advance ratio of 0.65 and 7000 *RPM*.

3.4.2 Aeronaut CAM Carbon Electric 13”X8” – 2 Blades

Results for the Aeronaut Carbon Electric 13”x8” 2 bladed propeller are shown in Fig. 9. It is possible to observe an increase in the thrust coefficient with the Reynolds number, but no significant changes are visible in the power coefficient. Consequently, the thrust increase leads to the typical increase in the

LRN propeller efficiency as the Reynolds number increases with propeller *RPM* .

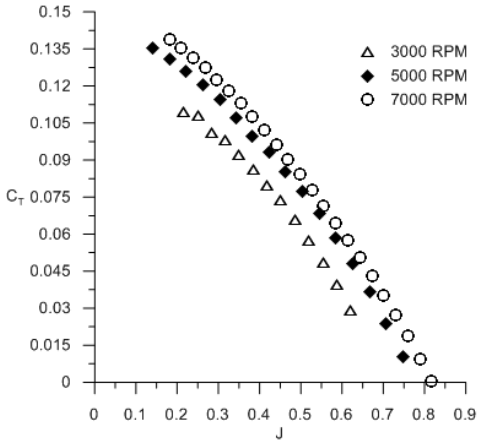

(a)

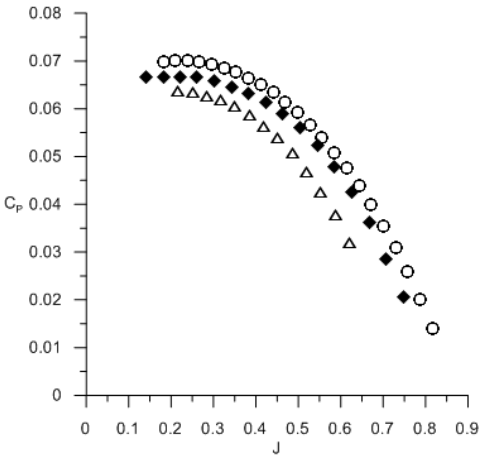

(b)

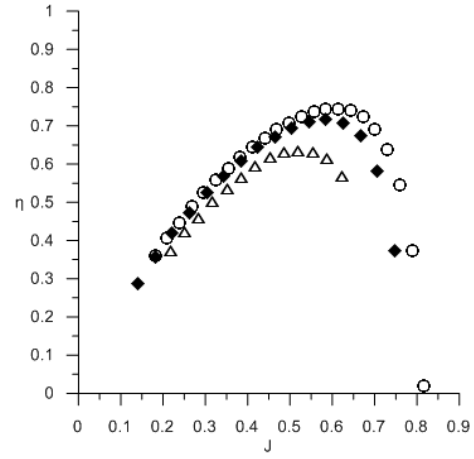

(c)

Fig. 8 – Aeronaut 12x8" Propeller data for 3000 *RPM*, 5000 *RPM* and 7000 *RPM* (a) thrust coefficient (b) power coefficient (c) propeller efficiency

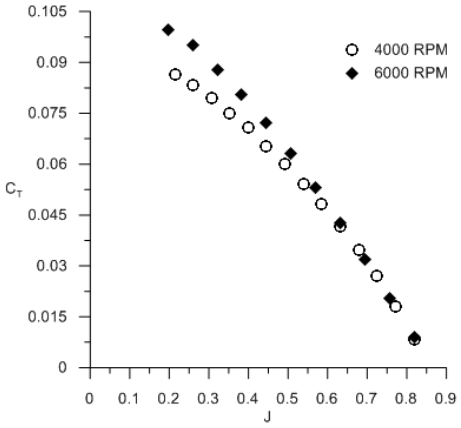

(a)

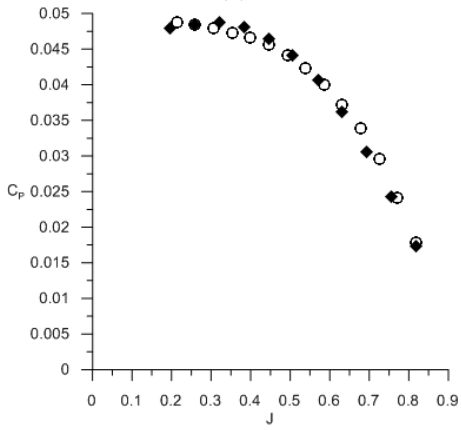

(b)

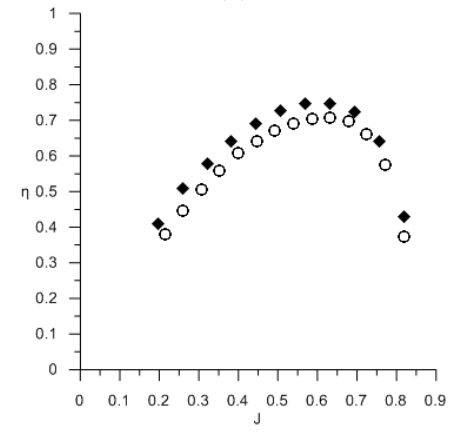

(c)

Fig. 9 – Aeronaut 13"x8" Propeller data for 4000 *RPM* and 6000 *RPM* (a) thrust coefficient (b) power coefficient (c) propeller efficiency

3.5 Uncertainty Analysis

The measurements error propagation begins with the primary quantities including thrust, torque, ambient pressure, temperature and tunnel flow rate static ports differential pressure. The purpose of the error analysis is to determine the level of precision of the presented propeller performance results. In order to execute the analysis it was assumed that there is no

error on the conversion from the sensor's voltages to the physical quantities; on the propeller diameter since it is given as a specification from the propeller manufacturer and on the wind tunnel sections dimensions since it is given as a specification from the manufacturer.

Although the manufacturers provide this uncertainty information about the sensors, all the primary readings experience some level of fluctuations. If the fluctuations in the measurement of parameter *X* have a normal distribution, then 95% of the samples will fall within ±2σ of the mean, so $\delta(X)=2\sigma$ can be applied [30]. The uncertainties analyzed include the wind tunnel freestream velocity, the propeller advance ratio, rotational speed, coefficients of thrust and power as well as the efficiency. A summary of the uncertainty analysis relative to the 12"x8" Aeronaut CAM Carbon folding 3-bladed propeller at 5000 *RPM* test is presented in the Table 1

Table 1 – Aeronaut 12"x8", 3 bladed Propeller uncertainty for 5000 *RPM* data

	Uncertainty				
V'	*V* [%]	*J* [%]	C_T [%]	C_P [%]	η [%]
4	2.834	0.186	0.193	0.463	2.874
5	3.833	0.178	0.173	0.446	3.859
6	2.533	1.744	3.363	3.376	3.126
7	1.480	0.176	0.267	0.502	1.576
8	0.817	0.170	0.245	0.477	0.964
9	0.891	0.166	0.181	0.450	1.003
10	0.551	0.177	0.222	0.520	0.758
11	0.617	0.167	0.236	0.468	0.791
12	0.420	0.163	0.203	0.493	0.660
13	0.334	0.166	0.235	0.540	0.654
14	0.380	0.173	0.332	0.606	0.755
15	0.309	0.171	0.332	0.654	0.765
16	0.376	0.173	0.539	1.407	1.533
17	0.273	0.171	0.926	0.854	1.267

It can be noted that:

- For freestream velocities around 5-6 *m/s* interval there is an increased uncertainty in the results. By analyzing the raw data, this appears to be a result of higher fluctuations on the measurements around this velocity interval;
- For freestream velocities above 7 *m/s*, the uncertainty in this parameter is less than 1%;
- The uncertainty in C_T is typically less than 0.3%;
- The uncertainty in C_P is typically less than 0.6%;
- The uncertainty in η is typically less than 1%.

The observed uncertainties prove to be small and, as expected, they increase as the predominant primary measurement decreases such as the uncertainty in freestream velocity which increases as P_{diff} measurements decrease. This increased uncertainty can be found at the 5-6 *m/s* freestream velocity interval for all the tests.

4 Conclusions

This paper has presented the development and validation of a new test rig, suitable to test a wide range of low Reynolds number propellers up to a diameter of about 14".

Furthermore, thrust and torque of 2 CAM Carbon, Aeronaut propellers were measured over a range of propeller advance ratios for different propeller rotational speeds.

It was shown that as the Reynolds number increases with the increase of propeller *RPM*, the propellers performance is affected by increasing their thrust coefficient and the efficiency.

The developed test rig can be used for several purposes, namely to improve the JBLADE Software.

Acknowledgements

The present work was performed as part of Project MAAT (Ref. No. 285602) supported by European Union through the 7th Framework Programme. Part of the work was also supported by C-MAST – Center for Mechanical and Aerospace Sciences and Technologies, Portuguese Foundation for Science and Technology Research Unit No. 151.

References:

[1] Z. Zheng, W. Huo, Z. Wu, Autonomous airship path following control: Theory and experiments, *Control Engeneering Practices* Vol. 21, 2013, pp. 769–788.

[2] Q. Wang, J. Chen, G. Fu, D. Duan, An approach for shape optimization of stratosphere airships based on multidisciplinary design optimization, *Journal of Zhejiang University Science A.* Vol. 10, 2009, pp. 1609–1616.

[3] E.H. van Eaton, Airships and the Modern Military, *U.S. Army War College*, Carlisle Barracks, 1991.

[4] L. Liao, I. Pasternak, A review of airship structural research and development, *Progress in Aerospace Sciences* Vol. 45, No. 4, 2009, pp. 83–96.

[5] J. Morgado, M.Â.R. Silvestre, J.C. Páscoa, Parametric Study of a High Altitude Airship According to the Multi-Body Concept for Advanced Airship Transport - MAAT, in: *IV Conferência Nacional em Mecânica Dos Fluidos, Termodinâmica e Energ*ia, Lisbon, 2012.

[6] Y.-G. Lee, D.-M. Kim, C.-H. Yeom, Development of Korean High Altitude Platform Systems, *International Journal of Wireless and Informatics and Networks*. Vol. 13, 2005, pp. 31–42.

[7] M.S. Smith, E.L. Rainwater, Applications of Scientific Ballooning Technology to High Altitude Airships, in: AIAA's *3rd Annual Aviation Technology Integration Operations and Technology Forum*, Denver, 1971: pp. 1–8.

[8] A. Dumas, M. Trancossi, M. Madonia, I. Giuliani, Multibody Advanced Airship for Transport, in: *Society of Automotive Engineers Technical Paper* 2011-01-2786, 2011.

[9] G. Ilieva, J.C. Páscoa, A. Dumas, M. Trancossi, A critical review of propulsion concepts for modern airships, *Central European Journal of Engineering.* Vol. 2, 2012, pp. 189–200.

[10] Lockheed Martin, High Altitude Airship (HAA) *Persistent Communications and ISR for the Joint Warfighter Partnering to Meet Customers' Defining Moments*, Defense.

[11] A. Colozza, B. Park, Initial Feasibility Assessment of a High Altitude Long Endurance Airship, 2003.

[12] A.C. Gawale, R.S. Pant, Initial Sizing and Sensitivity Analyses of Stratospheric Airships for Psuedolite Based Precision Navigation System, in: *5th ATIO and 16th Lighter-Than-Air Systems Technologies and Balloon Systems Conference*, American Institute of Aeronautics and Astronautics, Arlington, 2000, pp. 1–15.

[13] Egrett II Brochure, E-Systems GreenVille Division, 1991

[14] A. Colozza, High Altitude Propeller Design and Analysis Overview, *Technical Report* Cleveland, 1998.

[15] Merlin, P. W., "Crash Course - Lessons Learned from Accidents Involving Remotely Piloted and Autonomous Aircraft", *Monographs in Aerospace History #44*, National Aeronautics and Space Administration, 2013.

[16] M.A. Silvestre, J.P. Morgado, J. Pascoa, JBLADE: a Propeller Design and Analysis Code, *2013 International Powered Lift Conference*, American Institute of Aeronautics and Astronautics, Reston, Virginia, 2013.

[17] J. Morgado, M.A.R. Silvestre, J.C. Páscoa, Validation of New Formulations for Propeller Analysis, Journal of Propulsion and Power. DOI: 10.2514/1.B35240

[18] Drela, M., "XFOIL - An Analysis and Design System for Low Reynolds Number Airfoils", *Proceedings of Low Reynolds Number Aerodynamics*, Berlin, Vol. 54, 1989, pp. 1–12.

[19] M.S. Selig, Low Reynolds Number Airfoil Design Lecture Notes, *Von Kármán Institute*, 2003.

[20] T. Theodorsen, G.W. Stickle, M.J. Brevoort, Caracteristics of Six Propellers Including the High-Speed Range, *NACA Technical Report No. 594*, Langley, 1937.

[21] W. Gray, Wind-Tunnel Tests of Two Hamilton Standard Propellers Embodying Clark Y and Naca 16-Series Blade Sections, *NACA Technical Report No. 530*, Washington, 1941.

[22] R.W. Deters, G.K. Ananda, M.S. Selig, Reynolds Number Effects on the Performance of Small-Scale Propellers, *Procedings of 32nd AIAA Applied Aerodynamics Conference, A*merican Institute of Aeronautics and Astronautics, Atlanta, 2014.

[23] J.B. Brandt, M.S. Selig, Propeller Performance Data at Low Reynolds Numbers, (2011) 1–18.

[24] O.R. Shetty, M.S. Selig, Small-Scale Propellers Operating in the Vortex Ring State, in: 49th AIAA Aerosp. Sci. Meet. Incl. New Horizons Forum Aerosp. Expo., Orlando, Florida, 2011: pp. 1–16.

[25] Ananda, G., UIUC Propeller Database, Aerospace Engineering, *University of Illinois Champaign*, IL, http://aerospace.illinois .edu/m-selig/props/propDB.html [retrieved 25 September 2014].

[26] H. Glauert, Wind Tunnel Interference on Wings, Bodies, and Airscrews, 1933.

[27] A. Pope, J. Barlow, W. H. Rae, LOW-SPEED WIND TUNNEL TESTING, 1999.

[28] J.B. Brandt, SMALL-SCALE PROPELLER PERFORMANCE AT LOW SPEEDS, 2005.

[29] M.S. Selig, G. Ananda, Low Reynolds Number Propeller Perfomance Data : Wind Tunnel Corrections for Motor Fixture Drag, 2011.

[30] Hallauer W. L. Jr. and Devenport W. J., 2006, AOE 3054 Experimental Methods Course Manual. Experimental Error, A.O.E. Department, Virginia Tech. Blacksburg VA.